### Title
Toward Hydrogen Isotope Separations through Strong Hydrogen Adsorption at Open Copper(I) Sites in an Ultramicroporous Metal—Organic Framework




### Journal
Journal of the American Chemical Society, 148(24)

### ISSN
0002-7863



### Authors
Yabuuchi, Yuto
Furukawa, Hiroyasu
Klein, Ryan A
et al.



### Publication Date
2026-06-24

### DOI
10.1021/jacs.6c00512

# Toward Hydrogen Isotope Separations through Strong Hydrogen Adsorption at Open Copper(I) Sites in an Ultramicroporous Metal–Organic Framework

*Yuto Yabuuchi,[1,2,3] Hiroyasu Furukawa,[1,2,3] Ryan A. Klein,[1,2,4,5] Nikolay V. Tkachenko,[1,2,3,6] N. Isaac Zakaria,[2,3,7] Matthew N. Dods,[2,7] Sarah L. Karstens,[1,2,3] Hyun June Moon,[5,8] My K. Vuong,[1,2,3] Matthew S. Santoso,[2,7] Karina Riascos-Rodriguez,[9] Kurtis M. Carsch,[1,2] Hayden A. Evans,[5] Yongqiang Cheng,[10] Denis Shepytakov,[11] Karen C. Bustillo,[12] Andrew M. Minor,[12,13,] Walter S. Drisdell,[9] Martin Head-Gordon,[1,2,9] Craig M. Brown,[5 8] Jeffrey R. Long[1,2,3,7,13]*

[1]Department of Chemistry, University of California, Berkeley, California 94720, United States

[2]Baker Hughes Institute for Decarbonization Materials, University of California, Berkeley, California 94720, United States

[3]Materials Sciences Division, Lawrence Berkeley National Laboratory, Berkeley, California 94720, United States

[4]Material, Chemical, and Computational Sciences Directorate, National Renewable Energy Laboratory, Golden, Colorado 80401, United States

[5]Center for Neutron Research, National Institute of Standards and Technology, Gaithersburg, Maryland 20899, United States

[6]Department of Chemistry and Biochemistry, University of Oklahoma, Norman, Oklahoma 73019, United States

[7]Department of Chemical and Biomolecular Engineering, University of California, Berkeley, California 94720, United States

[8]Department of Chemical and Biomolecular Engineering, University of Delaware, Newark, Delaware 19716, United States

[9]Chemical Sciences Division, Lawrence Berkeley National Laboratory, Berkeley, California 94720, United States

[10]Neutron Scattering Division, Oak Ridge National Laboratory, Oak Ridge, Tennessee 37831, United States

[11]Laboratory for Neutron Scattering and Imaging, Paul Scherrer Institut, CH-5232 Villigen PSI, Switzerland

[12]National Center for Electron Microscopy, Molecular Foundry, Lawrence Berkeley National Laboratory, Berkeley, California 94720, United States

[13]Department of Materials Science and Engineering, University of California, Berkeley, California 94720, United States

*Email: jrlong@berkeley.edu

ABSTRACT

Metal–organic frameworks with coordinatively unsaturated metal sites (open metal sites) capable of engaging in orbital interactions with π-acidic gases are of interest for enabling ambient-temperature gas separations, such as hydrogen isotope separations. In view of the weakly π-acidic nature of $H_2$, we sought to strengthen π-backbonding-mediated $H_2$ adsorption through pore confinement effects. Toward that end, we synthesized and characterized the ultramicroporous metal–organic framework $Cu_xZn_{5-x}Cl_{4-y}H_z(bbta)_3$ ($Cu^I$Zn-MFU-4; $H_2$bbta = 1*H*,5*H*-benzo(1,2-*d*:4,5-*d*′)bistriazole), featuring π-basic trigonal pyramidal $Cu^I$ sites that reside within 7 Å at the closest of one another. Gas adsorption measurements reveal an $H_2$ adsorption enthalpy of −38 kJ/mol, exceeding that of the larger-pore analog ($Cu^I$Zn-MFU-4*l*; −33 kJ/mol) and representing the strongest $H_2$ adsorption yet achieved in a metal–organic framework. The stronger $H_2$ adsorption in $Cu^I$Zn-MFU-4 is attributed to a combination of pore confinement effects and the increased σ-accepting nature of the $Cu^I$ sites caused by a more electron-withdrawing $bbta^{2-}$ linker, as supported by structural, spectroscopic, and computational evidence. With the strongest $H_2$ adsorption, equilibrium isotope effects in $Cu^I$Zn-MFU-4 lead to a $D_2/H_2$ selectivity (as estimated by ideal adsorbed solution theory) of 1.35 even at 298 K, approaching the values reported below 200 K for conventional porous materials.

## INTRODUCTION

Metal–organic frameworks (MOFs) are crystalline, porous adsorbents that can be synthetically tuned by deliberately selecting specific metal nodes and organic linkers to realize diverse pore sizes and three-dimensional structures with well-defined surface functionalities.[1] One of the key functionalities in metal–organic frameworks is coordinatively unsaturated metal sites (also known as open metal sites).[2,3] When a small molecule is adsorbed at an open metal site through coordination interactions, it can exhibit stronger and more selective adsorption than typical physisorption, which relies on van der Waals interactions. The synthetic tunability of open metal sites in such porous solid materials makes them promising candidates for various applications, including gas storage and separations,[4,5] catalysis,[6,7] and sensing.[8–10]

While typical open metal sites in metal–organic frameworks are recognized as Lewis acids that primarily adsorb gas molecules through polarization due to their cationic charge,[11] some frameworks with π-basic metal sites have been shown to adsorb π-acidic gas molecules, such as $H_2$ and $N_2$, via orbital interactions (i.e., π-backbonding). Gas adsorption via orbital interactions in these frameworks is stronger than that with Lewis acidic metal sites, leading to a significant enhancement in π-acidic gas uptake compared to adsorbents without orbital interactions.[12–14] Furthermore, because π-backbonding interactions occur exclusively with π-acidic molecules, π-basic metal sites can exhibit gas selectivity that is difficult to achieve with traditional adsorbents, which typically differentiate gases based on their kinetic diameter or polarizability.[12]

Among metal–organic frameworks with π-basic metal sites,[12–16] the frameworks $Cu_nM_{5-n}X_{4-n}(btdd)_3$ ($Cu^IM$-MFU-4*l*, where *l* stands for large; M = Zn, Mn, Cd; X = Cl, I; $H_2$btdd = bis(*1*H-1,2,3-triazolo)-[4,5-*b*],[4′,5′-*i*]dibenzo[1,4]dioxin)[14,16] with trigonal pyramidal $Cu^I$ sites drew our attention for understanding the critical factors that control their π-backbonding-mediated

gas adsorption. The MFU-4*l* class of frameworks features a primitive cubic net with pentanuclear cluster nodes connected by linear bistriazolate linkers (Figure 1).[14,17] Each pentanuclear cluster contains one octahedral metal ion in the central position and four pseudo-tetrahedral metal ions at peripheral sites. Although MFU-4*l* itself ($Zn_5Cl_4(btdd)_3$, hereafter referred to as ZnCl-MFU-4*l*) is composed of $Zn^{II}$ ions,[17] various post-synthetic modifications such as metal-exchange and anion-exchange for the peripheral $Zn^{II}$–Cl moieties have been employed to introduce desired metal species into the framework.[16,18,19]

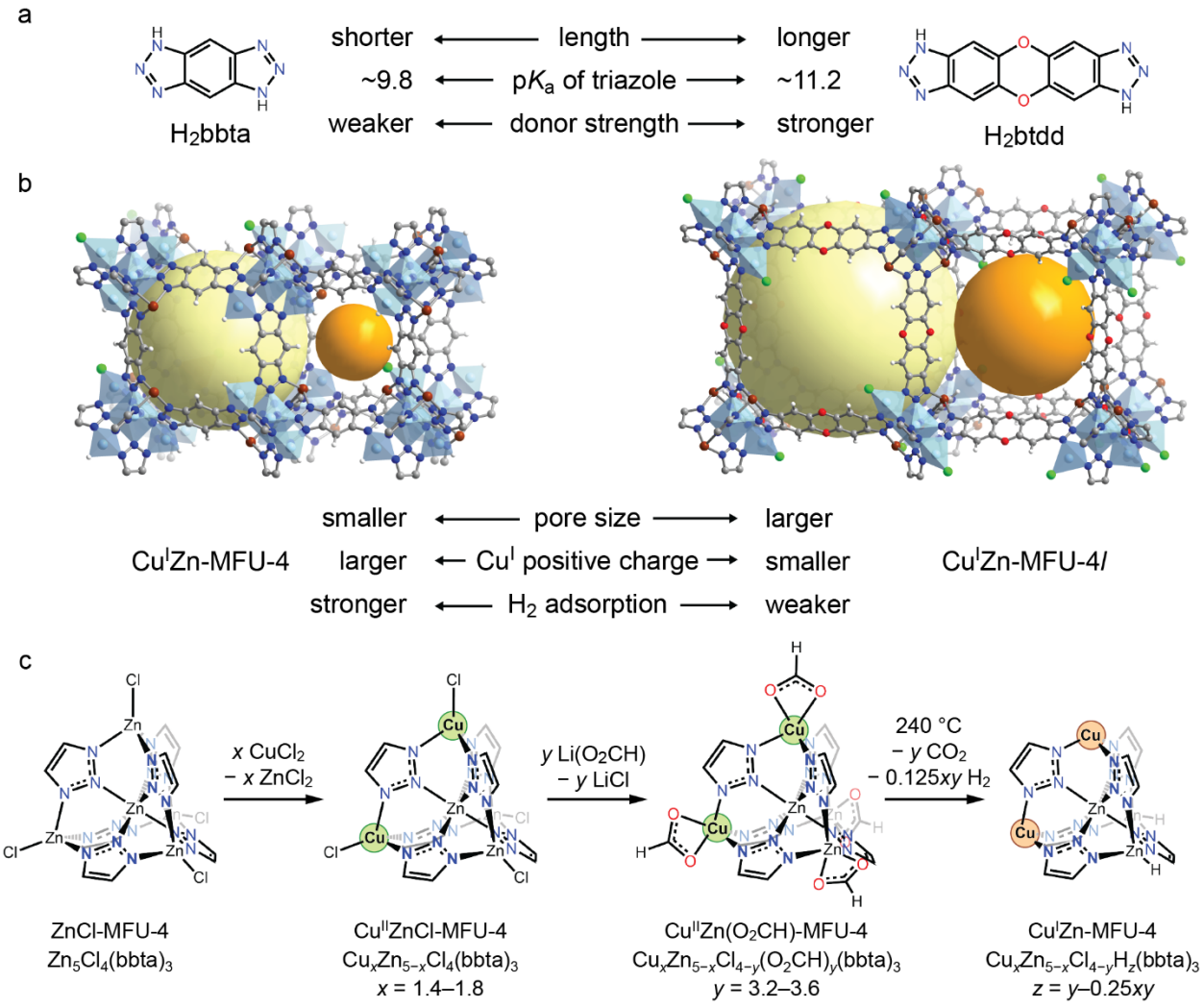

**Figure 1.** (a) The structures of $H_2$bbta and $H_2$btdd linkers, and comparison of their properties. The p$K_a$ values were calculated using Rowan's method.[20] (b) Portions of the crystal structures of $Cu^I$Zn-MFU-4 and $Cu^I$Zn-MFU-4*l*[21] obtained through Rietveld refinement of powder neutron diffraction patterns. Gray, blue, red, white, brown, light blue, and green spheres represent C, N, O, H, Cu, Zn, and Cl atoms, respectively. Yellow and orange spheres represent larger and smaller pores, respectively, as guides to the eye. (c) Post-synthetic modifications of the cluster nodes in ZnCl-MFU-4 to generate $Cu^I$Zn-MFU-4.

One of the most investigated variants of functionalized MFU-4*l* is $Cu^I$-MFU-4*l* (hereafter referred to as $Cu^I$Zn-MFU-4*l*),[16] which has trigonal pyramidal $Cu^I$ sites at approximately two of the peripheral sites. The π-basic $Cu^I$ sites facilitate various gas separations, including selective capture of olefin over paraffin gases,[22] oxygen separation from air,[23] and nitrogen removal from natural gas.[24] Recently, we reported that the π-basicity of the $Cu^I$ sites in $Cu^I$M-MFU-4*l* can be systematically altered by replacing the $M^{II}$ (M = Zn, Mn, Cd) ion at the center of the pentanuclear cluster.[14,25] The strength of π-backbonding depends on the pyramidal geometry of the $Cu^I$ sites, with the strongest $Cu^I$–$H_2$ interactions observed in $Cu^I$Zn-MFU-4*l*.

Although the control of π-basicity at the trigonal $Cu^I$ sites is achieved by altering their first coordination sphere, we sought to investigate whether we can further strengthen $H_2$ adsorption at these sites by a unique tuning parameter that is not present in molecular coordination complexes: pore size. In the gas adsorption literature, it is established that porous materials with pore apertures below 7 Å, known as ultramicropores, generally physisorb gases more strongly than materials with larger pores.[26–29] Such an enhancement of adsorption within ultramicropores is thought to be due to pore confinement effects,[30,31] which are caused by the overlap of adsorption potentials of

different sides of the pore to deepen and sharpen the overall potential well.[32,33] Because the pores of $Cu^{I}$Zn-MFU-4*l* are too large to induce pore confinement effects, we sought to introduce open $Cu^{I}$ sites in a framework with a shorter linker to investigate whether pore confinement effects can influence orbital-interaction-mediated gas adsorption.

The importance of achieving strong, reversible $H_2$ adsorption is underscored by the challenge of hydrogen isotope separations ($D_2$, HD, $H_2$, etc.) due to the similar properties of these isotopes. Currently, the most common approach to these separations involves cryogenic distillation, which is conducted at extremely low temperatures due to the boiling points of these diatomic molecules near 20 K.[34,35] With deuterium demand expected to rise in the semiconductor industry,[36,37] medicinal chemistry,[38] and nuclear power technology,[39,40] the need for an energy-efficient separation process for deuterium is escalating. For developing porous materials with hydrogen isotope separations, one popular strategy entails the design of pore apertures comparable to the de Broglie wavelength of an $H_2$ molecule to capitalize on kinetic quantum sieving (KQS).[41–43] Although this mechanism is effective below 50 K, the de Broglie wavelength of an $H_2$ molecule is inversely dependent on temperature to significantly decrease the selectivity at temperatures above 70 K.[43,44] A complementary approach uses chemical affinity quantum sieving (CAQS) in adsorbents with strong $H_2$ adsorption sites to exploit the thermodynamic preference for adsorption of heavier isotopologues arising from differences in zero-point energy.[45–47] These two strategies, individually or in combination, realized outstanding $D_2/H_2$ selectivity. However, most porous adsorbents have been evaluated only at cryogenic temperatures, typically below 100 K. Weak $H_2$ adsorption in porous materials generally limits uptake to less than 0.1 mmol/g at ambient conditions (298 K, 1 bar),[48] hindering explorations toward separations under these more favorable conditions. Achieving strong yet reversible $H_2$ adsorption could enable isothermal processes for

hydrogen isotope separations at room temperature, significantly reducing energy costs by eliminating large temperature swings during adsorption and desorption.

Because molecular $H_2$ complexes are known to favor $D_2$ binding over $H_2$ binding through equilibrium isotope effects (also referred to as "chemical affinity quantum sieving" in recent porous adsorbent studies)[49] even at ambient temperatures,[50–53] strong $H_2$ adsorption in metal–organic frameworks should induce thermodynamic selectivity toward heavier isotopologues under these conditions. Furthermore, the permanent porosity of metal–organic frameworks provides a higher density of accessible metal sites and facile gas diffusion, overcoming limitations of molecular complexes.[54,55] Strengthening $H_2$ adsorption to increase gas capacity may also enhance $D_2/H_2$ selectivity, given an empirical relationship between $H_2$ adsorption enthalpy and $D_2/H_2$ selectivity in porous materials.[49,50,56] In view of the mechanism of equilibrium isotope effects, π-backbonding interactions have opposing effects on zero-point energy around metal–$H_2$ vibrations by lowering the H–H stretching energy while increasing energies of the librational and torsional modes of $H_2$ due to increased metal–hydride bond character.[50,51] Strengthening $H_2$ adsorption at π-basic metal sites through pore confinement and examining its influence on equilibrium isotope effects ($D_2/H_2$ selectivity) can inform the material design strategy for hydrogen isotope separations.

Here, we report the synthesis and characterization of the metal–organic framework $Cu^{I}$Zn-MFU-4 ($Cu_xZn_{5-x}Cl_{4-y}H_z(bbta)_3$; $H_2$bbta = 1*H*,5*H*-benzo(1,2-*d*:4,5-*d*′)bistriazole), which is isoreticular to $Cu^{I}$Zn-MFU-4*l* with a shorter neighboring $Cu^{I}\cdots Cu^{I}$ distance in the pore (~7 Å, Figure 1b). Through gas adsorption measurements, we show that this compound exhibits the largest $H_2$ adsorption enthalpy of −38 kJ/mol among porous framework materials. *In situ* spectroscopy, diffraction studies, and computational analyses suggest that enhancement of $H_2$ adsorption in

$Cu^{I}$Zn-MFU-4 compared to $Cu^{I}$Zn-MFU-4*l* arises from a combination of pore confinement effects and the increased σ-accepting nature of the $Cu^{I}$ sites. We further evaluate thermodynamic and kinetic differences between $H_2$, HD, and $D_2$ adsorption at ambient temperatures in $Cu^{I}$Zn-MFU-4. Finally, we conduct a preliminary assessment describing how $Cu^{I}$Zn-MFU-4 might be utilized to implement hydrogen isotope separations at ambient temperatures by repetitive enrichment, as illustrated with a McCabe–Thiele diagram[57,58] combined with the ideal adsorbed solution theory.[59]

## EXPERIMENTAL SECTION

Detailed synthetic and characterization procedures for the frameworks, along with computational details, are provided in the Supporting Information (SI). The compounds ZnCl-MFU-4*l*,[17] $Cu^{I}$Zn-MFU-4*l*,[23] and ZnCl-MFU-4[60] were synthesized following a previously reported procedure.

**Synthesis of $Cu_xZn_{5-x}Cl_4(bbta)_3$ ($Cu^{II}$ZnCl-MFU-4).** Desolvated ZnCl-MFU-4 (0.100 g, 0.106 mmol, 1.00 equiv.) was suspended in a solution of copper(II) chloride (0.713 g, 5.30 mmol, 50.0 equiv.) in 20 mL of methanol at 55 °C for 10 days. The supernatant was decanted and the product was washed with methanol at 55 °C for 6 h. This procedure was repeated eight times. For isolation of the product, the resulting orange powder was collected by filtration. The resulting material was further desolvated by heating at 180 °C for 24 h under dynamic vacuum, yielding 0.063 g (63% yield) of guest-free microcrystalline powder. The typical *x* value is 1.4–1.8 with an average of 1.6. Elemental analysis calcd for $Cu_{1.6}Zn_{3.4}Cl_4(C_6H_2N_6)_3$: C, 23.00%; H, 0.64%; N, 26.82%. Found: C, 22.78%; H, 0.71%; N, 26.14%.

**Synthesis of $Cu_xZn_{5-x}Cl_{4-y}(O_2CH)_y(bbta)_3$ ($Cu^{II}$Zn($O_2$CH)-MFU-4).** The methanol-solvated $Cu^{II}$ZnCl-MFU-4 powder from the above procedure prior to desolvation was suspended in 20 mL

of a methanol solution containing lithium formate monohydrate (0.742 g, 10.6 mmol, 100 equiv.). The mixture, contained in a capped 20-mL vial, was allowed to stand without stirring at 25 °C for 6 days, during which the supernatant was decanted and freshly replenished after 3 days. Following this, the supernatant was decanted and the product was washed with methanol at 25 °C for 6 h. This procedure was repeated eight times. The resulting yellow powder was collected by filtration and dried under dynamic vacuum at room temperature for 1 h, followed by heating at 60 °C for 6 h. The product was subsequently dried at 80 °C for 48 h to afford 0.084 g of the orange-gold microcrystalline powder (82% yield based on the starting ZnCl-MFU-4 material). The typical *y* value is 3.2–3.6 with an average of 3.4. Elemental analysis calcd for $Cu_{1.6}Zn_{3.4}Cl_{0.6}(O_2CH)_{3.4}(C_6H_2N_6)_3$: C, 26.43%; H, 0.97%; N, 25.92%. Found: C, 26.40%; H, 1.05%; N, 25.36%.

**Synthesis of $Cu_xZn_{5-x}Cl_{4-y}H_z(bbta)_3$ ($Cu^{I}Zn$-MFU-4).** The desolvated $Cu^{II}Zn(O_2CH)$-MFU-4 powder was slowly heated to 240 °C under dynamic vacuum (see a detailed procedure in the SI), followed by continuous heating at 240 °C under dynamic vacuum for 48 h to yield 0.072 g of product as a dark orange powder (quantitative yield from $Cu^{II}Zn(O_2CH)$-MFU-4). The *z* value is calculated by $z = y - 0.25xy$. Elemental analysis calcd for $Cu_{1.6}Zn_{3.4}Cl_{0.6}H_{2.0}(bbta)_3$: C, 26.31%; H, 0.98%; N 30.69%. Found: C, 26.16%; H, 0.96%; N, 29.48%.

## RESULTS AND DISCUSSION

The metal–organic framework $Zn_5Cl_4(bbta)_3$ (ZnCl-MFU-4)[60] is isoreticular with $Zn_5Cl_4(btdd)_3$ (ZnCl-MFU-4*l*),[17] but contains a shorter linker (Figure 1). The $bbta^{2-}$ linkers run parallel to each crystallographic axis while alternating the angle of the aromatic plane by 90°. This linker arrangement results in two distinct types of pores alternating within MFU-4-type frameworks

(Figure 1b). Both cubic pores are defined by twelve $bbta^{2-}$ linkers at the edges and eight pentanuclear cluster nodes at the corners. However, the peripheral metal species of the cluster nodes (i.e., $Zn^{II}$–Cl sites) point only toward the center of the smaller pore, creating a pore aperture with a diameter of just ~2.5 Å, as measured by the available room surrounded by $Zn^{II}$–Cl sites with their van der Waals radii.[60] This small pore aperture has been cited as the reason underlying unsuccessful attempts to post-synthetically substitute the metal ions in ZnCl-MFU-4,[18,24,61] despite multiple reports on post-synthetic metal-exchange for the larger pore analog, ZnCl-MFU-4*l*.[16,18,19] Yet, reports demonstrating post-synthetic anion-exchange in ZnCl-MFU-4[62] appear to contradict this diffusion-limiting small pore hypothesis, which prompted us to further investigate the feasibility of $Cu^{II}$-exchange in ZnCl-MFU-4, after which reduction of $Cu^{II}$ could be adapted from the procedure for $Cu^{I}$Zn-MFU-4*l*.[16]

**Synthesis of $Cu^{I}$Zn-MFU-4.** By screening of exchange conditions, we found that using a polar protic solvent (specifically, methanol) is important for achieving successful $Cu^{II}$-exchange in ZnCl-MFU-4 (Table S4). In contrast, the use of aprotic solvents, such as *N*,*N*-dimethylformamide or *N*,*N*-dimethylacetamide, which are often used for metal-exchange in other MFU-4-type frameworks,[18,19,63,64] resulted in a low extent of $Cu^{II}$ incorporation.

The crystallinity, phase purity, and porosity of the $Cu^{II}$-exchanged product (hereafter termed $Cu^{II}$ZnCl-MFU-4) were confirmed using powder X-ray diffraction analysis, scanning electron microscopy (SEM) observations, and $CO_2$ adsorption measurements at 195 K (see the SI for complete characterizations). The Cu:Zn ratio in the framework was estimated to be 1.6:3.4 on average using inductively coupled plasma optical emission spectroscopy (ICP-OES) for $Cu^{II}$ZnCl-MFU-4 after acidification to achieve a homogeneous solution. Upon successfully exchanging ZnCl-MFU-4 with $Cu^{II}$, the $Cu^{II}$ sites were reduced to form coordinatively unsaturated $Cu^{I}$ sites

with a trigonal pyramidal geometry, as shown in Figure 1c.[16,23] In brief, the peripheral chloride anion was exchanged with a formate anion, and subsequently peripheral $Cu^{II}$–$O_2CH$ and $Zn^{II}$–$O_2CH$ sites were thermolyzed to yield open trigonal $Cu^{I}$ sites and $Zn^{II}$–H species.

The resultant framework, which we denote as $Cu^{I}$Zn-MFU-4, exhibited a Type-I adsorption isotherm for $N_2$ at 77 K (Figure S12), with Brunauer–Emmet–Teller (BET) and Langmuir surface areas of 1370 and 1530 $m^3/g$, respectively (Table 1). The micropore volume of 0.54 $cm^3/g$ is also close to the expected value from its modeled structure, within a 10% difference. The facile gas accessibility to the pores in $Cu^{I}$Zn-MFU-4 suggests larger pore apertures than those of ZnCl-MFU-4, consistent with the presence of terminal $Zn^{II}$–H species and coordinatively unsaturated $Cu^{I}$ sites. The gas accessibility in $Cu^{I}$Zn-MFU-4 sharply contrasts with the parent frameworks ZnCl-MFU-4, $Cu^{II}$ZnCl-MFU-4, and $Cu^{II}Zn(O_2CH)$-MFU-4, where the experimentally obtained $N_2$ or Ar uptake at 77 K or 87 K was much lower than expected due to the small pore aperture (~2.5 Å), which hinders gas diffusion.[60] However, the use of $CO_2$, with a smaller kinetic diameter than $N_2$ and Ar ($CO_2$: ~3.3 Å, $N_2$: 3.64 Å, Ar: 3.40 Å),[65,66] allowed the evaluation of the porosity of these precursor frameworks to ensure the structural integrity after each post-synthetic modification (Tables 1 and S12).

**Table 1. Summary of Surface Areas, Pore Volumes, Unit Cell Parameters, and Isosteric Enthalpies of $H_2$ Adsorption for MFU-4 and MFU-4*l* Frameworks**

| material | surface area ($m^2/g$) | | | pore volume ($cm^3/g$) | | *a* (Å)[c] | $-\Delta H_{ads}$ at 0.5 mmol/g (kJ/mol)[d] | reference |
|---|---|---|---|---|---|---|---|---|
| | BET | Langmuir (obsd.) | Langmuir (calcd.)[a] | DR (obsd.)[b] | calcd. | | | |
| ZnCl-MFU-4[e] | 1030 | 1180 | 1260 | 0.43 | 0.46 | 21.67589(3) | 7.1 (77–87 K) | this work |
| $Cu^{I}$Zn-MFU-4 | 1370 | 1530 | 1620 | 0.54 | 0.58 | 21.67178(8) | 37.8 (278–318 K) | this work |

| | | | | | | | | |
|---|---|---|---|---|---|---|---|---|
| ZnCl-MFU-4*l* | 3470 | 3880 | 3990 | 1.38 | 1.42 | 31.0736(5) | 6.5 (77–87 K) | [14] |
| $Cu^{I}$Zn-MFU-4*l* | 3660 | 4080 | 4470 | 1.45 | 1.59 | 31.1286(5) | 33.1 (278–318 K) | this work |
| | | | | | | | 33.4 (223–263 K) | [14] |
| | | | | | | | 32 (163–193 K) | [16] |

[a]Calculated based on the available free volume of a model structure, assuming monolayer formation of probe molecules ($N_2$ or $CO_2$) within the pore and using the cross-sectional area of the probe molecule (further details are provided in the SI). [b]Pore volume estimated by the Dubinin–Radushkevich (DR) method. [c]Cubic lattice parameter obtained by Pawley fit for a powder X-ray diffraction pattern collected at 298 K. Values in parentheses indicate error bars as ±1σ. [d]Isosteric enthalpy of $H_2$ adsorption estimated by the Clausius–Clapeyron method at an $H_2$ loading of 0.50 mmol/g. Numbers in parentheses indicate the temperature range of the adsorption isotherm data [e]Surface areas and pore volumes were examined with $CO_2$ at 195 K.

The formation of trigonal pyramidal $Cu^{I}$ sites in $Cu^{I}$Zn-MFU-4 was confirmed by Cu K-edge X-ray absorption spectroscopy (Figure 2). Specifically, the X-ray absorption near-edge fine structure (XANES) of $Cu^{I}$Zn-MFU-4 lacks the quadrupolar 1s→3d pre-edge resonance diagnostic of formally $Cu^{II}$ species,[67] which was observed for $Cu^{II}$ZnCl-MFU-4 at ~8978 eV. The XANES for $Cu^{I}$Zn-MFU-4 additionally reveals a rising-edge feature around ~8983 eV, which was observed for $Cu^{I}$Zn-MFU-4*l* albeit differing intensity and not observed in $Cu^{II}$ZnCl-MFU-4. This feature is primarily due to transitions into the low-lying $4p_z$ orbital of trigonal $Cu^{I}$ sites. The lower intensity of this feature for $Cu^{I}$Zn-MFU-4 than for $Cu^{I}$Zn-MFU-4*l* implies the more pyramidal geometry of the $Cu^{I}$ sites in $Cu^{I}$Zn-MFU-4. The more pyramidal $Cu^{I}$ sites could exhibit greater overlap between the Cu $4p_z$ orbital and triazolate donor orbitals, leading to greater metal–ligand orbital mixing and lowering the 1s→$4p_z$ transition probability.

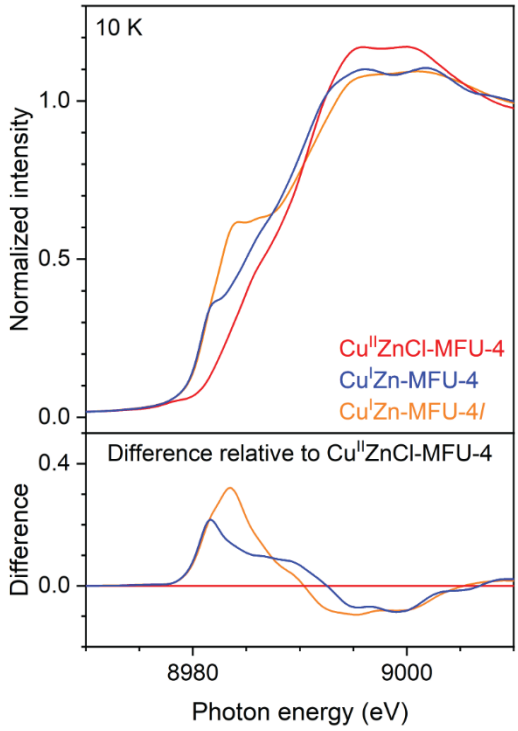


**Figure 2.** Copper K-edge X-ray absorption spectra for $Cu^{II}$ZnCl-MFU-4 (red), $Cu^{I}$Zn-MFU-4 (blue), and $Cu^{I}$Zn-MFU-4*l* (orange) collected at 10 K. Difference spectra with respect to the $Cu^{II}$ZnCl-MFU-4 spectrum are shown at the bottom to illustrate the energy alignment and the relative intensity of the rising-edge feature arising from trigonal $Cu^{I}$ sites for $Cu^{I}$Zn-MFU-4 and $Cu^{I}$Zn-MFU-4*l*.

**$H_2$ Adsorption Properties.** We expected that the formation of open trigonal $Cu^{I}$ sites would enable strong $H_2$ adsorption at the $Cu^{I}$ sites in $Cu^{I}$Zn-MFU-4.[14,16,23] To test this hypothesis, low-pressure $H_2$ adsorption isotherms were collected at 77 K. Because almost all accessible $Cu^{I}$ sites are expected to be occupied by $H_2$ at 1 mbar and 77 K, the $H_2$ uptake under these conditions should reflect the density of active $Cu^{I}$ sites in the framework.[23] As anticipated, steep $H_2$ uptake was observed below 1 mbar at 77 K, which is reminiscent of the $H_2$ adsorption profiles of $Cu^{I}$M-MFU-4*l* frameworks (Figure S23).[14,23] The steep increase in $H_2$ uptake in $Cu^{I}$Zn-MFU-4 reaches 1.3

mmol/g at 1 mbar, equivalent to approximately 90% of the expected uptake for 1 $H_2$ per $Cu^I$ based on the formula unit of $Cu_{1.6}Zn_{3.4}Cl_{0.6}H_{2.0}(bbta)_3$. As a reference, we collected $H_2$ adsorption isotherms for the parent ZnCl-MFU-4 framework and two Cu(II)-exchanged frameworks (i.e., $Cu^{II}$ZnCl-MFU-4 and $Cu^{II}Zn(O_2CH)$-MFU-4). These parent and intermediate MFU-4 frameworks exhibited Type-I adsorption profiles upon $H_2$ adsorption due to the smaller kinetic diameter of $H_2$ (2.89 Å),[65,66] unlike $N_2$ adsorption at 77 K. The frameworks did not show a significant $H_2$ uptake below 1 mbar at 77 K (Figure S23). This finding suggests that the strong $H_2$ adsorption sites are obtained only following the autoreduction of the $Cu^{II}$–$O_2CH$ sites to $Cu^I$. Notably, $Cu^I$Zn-MFU-4 retained its open $Cu^I$ sites, crystallinity, and porosity after exposure to water vapor or air, as supported by $H_2$ and $N_2$ adsorption isotherms and powder X-ray diffraction analyses (Figures S76–S85; see the SI for additional information).

Although $H_2$ uptake at 1 mbar and 77 K can be a useful measure of the density of $Cu^I$ sites available for strong gas adsorption, the initial slope of the isotherm at this temperature is too steep to compare the adsorption strength with other reported frameworks with open $Cu^I$ sites. Therefore, we collected the $H_2$ adsorption isotherm for $Cu^I$Zn-MFU-4 at 298 K, enabling an easier comparison of the $H_2$ adsorption strength with that of the expanded analog, $Cu^I$Zn-MFU-4*l* (Figure 3a). The slope of the $H_2$ isotherm for $Cu^I$Zn-MFU-4 is steeper than that of $Cu^I$Zn-MFU-4*l* below 0.1 bar at 298 K, indicating stronger $H_2$ adsorption at the $Cu^I$ site in $Cu^I$Zn-MFU-4 compared to the $Cu^I$ sites in $Cu^I$Zn-MFU-4*l*. High-pressure adsorption isotherm data revealed a volumetric excess $H_2$ uptake of 7.5 g/L for $Cu^I$Zn-MFU-4 at 100 bar and 298 K (Figure S71), which is ~80% greater than that of $Cu^I$Zn-MFU-4*l* and exceeds that of any other porous adsorbent under these conditions (Table S23), thus demonstrating high gas densification effects within the pores.

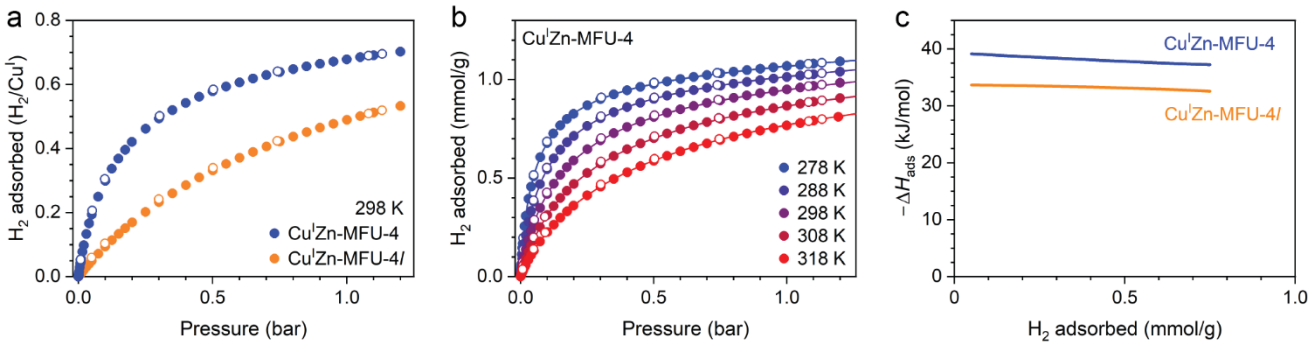


**Figure 3.** Low-pressure $H_2$ adsorption isotherms for $Cu^{I}$Zn-MFU-4 (blue) and $Cu^{I}$Zn-MFU-4*l* (orange) at 298 K (a), and $H_2$ adsorption isotherms for $Cu^{I}$Zn-MFU-4 collected in 10 K intervals from 278 to 318 K (b). Filled and open circles represent adsorption and desorption data, respectively. Solid lines represent fit to the triple-site Langmuir–Freundlich model. (c) Isosteric enthalpy of $H_2$ adsorption in $Cu^{I}$Zn-MFU-4 (blue) and $Cu^{I}$Zn-MFU-4*l* (orange) calculated by the Clausius–Clapeyron method.

To evaluate the $Cu^{I}$–$H_2$ interaction more quantitatively, the isosteric enthalpy of $H_2$ adsorption ($\Delta H_{ads}$, also referred to as the isosteric heat of adsorption, $-Q_{st}$) for $Cu^{I}$Zn-MFU-4 was estimated by collecting $H_2$ adsorption isotherms at multiple temperatures. The adsorption isotherms collected between 278 and 318 K were fit using a triple-site Langmuir–Freundlich model to obtain the pressure for the specific $H_2$ loading in the framework, allowing the Clausius–Clapeyron analysis to calculate $\Delta H_{ads}$ values (Figure 3b). The plot of the logarithm of pressure versus the reciprocal temperature (i.e., ln $P$ vs. $1/T$, known as a Clausius–Clapeyron plot) shows excellent linearity with the slope corresponding to $-\Delta H_{ads}/R$, where $R$ is the gas constant (Figure S34). This trend indicates minimal temperature dependence of $\Delta H_{ads}$ across this relatively large temperature range (40 K) and the small errors in the linear regression analysis. The slopes of the Clausius–Clapeyron plots appear nearly parallel for different $H_2$ loadings until reaching the maximum $H_2$ loading, indicating

a constant $\Delta H_{ads}$ until saturation of the $Cu^{I}$ sites, which suggests that each Cu–$H_2$ adsorption event can be considered as approximately independent. The resultant $\Delta H_{ads}$ value derived from the slope is −37.8 kJ/mol at 0.5 mmol/g, with a slight decreasing trend from −39.1 to −37.2 kJ/mol across $H_2$ loading of 0.05 to 0.75 mmol/g within the examined temperature range of 278–318 K.

The magnitude of $\Delta H_{ads}$ for $Cu^{I}$Zn-MFU-4 is ~5 kJ/mol larger than that of $Cu^{I}$Zn-MFU-4*l* (−33 kJ/mol; Figure 3c),[14,16] reflecting the largest reported $H_2$ adsorption enthalpy among reported porous materials. The 5 kJ/mol difference in $\Delta H_{ads}$ between $Cu^{I}$Zn-MFU-4 and $Cu^{I}$Zn-MFU-4*l* is relatively large and unusual, as $H_2$ adsorption enthalpies are often insensitive to the first coordination sphere, even upon changing the ligand identity for typical Lewis acidic open metal sites.[11,63,68,69] Furthermore, changing the bistriazolate linker from $btdd^{2-}$ to $bbta^{2-}$ does not significantly change $\Delta H_{ads}$ between the hexagonal frameworks $Ni_2Cl_2$(btdd) and $Ni_2Cl_2$(bbta) (−7.6 kJ/mol[63] vs. −7.5 kJ/mol (Figure S30), respectively), both of which feature Lewis acidic $Ni^{II}$ sites. Compared to the negligible change in $\Delta H_{ads}$ between $Ni_2Cl_2$(bbta) and $Ni_2Cl_2$(btdd), the response of $\Delta H_{ads}$ at trigonal $Cu^{I}$ sites in $Cu^{I}$Zn-MFU-4 and $Cu^{I}$Zn-MFU-4*l* frameworks is much more significant. In the following sections, we will elucidate the origin of the larger $\Delta H_{ads}$ in $Cu^{I}$Zn-MFU-4.

***In Situ* $D_2$-Dosing Powder Neutron Diffraction.** To examine structural differences in $Cu^{I}$–$H_2$ interactions between $Cu^{I}$Zn-MFU-4 and $Cu^{I}$Zn-MFU-4*l*, powder neutron diffraction experiments with *in situ* $D_2$-dosing were performed for $Cu^{I}$Zn-MFU-4 (further details are provided in the SI).[70] We chose $D_2$ as a probe gas molecule instead of $H_2$ for powder neutron diffraction analyses due to the very large incoherent scattering cross section of $^1H$ that typically strongly affects the background. Although a quantum rotation of the $D_2$ molecule precludes the accurate determination of the positions of its individual atoms, the $D_2$ adsorption sites can be located by the super atom

approach,[14,21,71,72] in which a single $D_2$ molecule was represented as one super atom capable of having up to twice occupancy and a large displacement parameter. In this work, we first collected diffraction data for activated $Cu^{I}$Zn-MFU-4 to obtain the gas-free structure at ~1.5 K. The sample was subsequently warmed to 80 K and dosed with 0.75 equivalents of $D_2$ per $Cu^{I}$, and equilibrated at 80 K. The sample was then recooled to 1.5 K to obtain a diffraction pattern under 0.75 equivalents of $D_2$. This procedure was repeated to collect diffraction patterns under dosing conditions of 1.5 and 2.5 equivalents of $D_2$.

Pawley fits against the collected diffraction patterns revealed a decrease in the lattice parameter by ~0.055(2) Å between the activated framework at 1.5 K and the framework under 0.75 equivalents of $D_2$ at 1.5 K (Figure S58). The lattice parameter did not further change significantly under 1.5 equivalents of $D_2$. Such lattice contraction upon gas binding was also observed during non-dissociative $D_2$ chemisorption at the $Cu^{I}$ sites, as reported in our previous powder neutron diffraction study of the $Cu^{I}$M-MFU-4*l* (M = Zn,[21] Mn[14]) frameworks. This phenomenon has been attributed to an increase in the degree of pyramidalization of the $Cu^{I}$ sites upon $H_2$ binding.[21]

To obtain the atomic-scale structure of gas-free $Cu^{I}$Zn-MFU-4, the diffraction pattern for activated $Cu^{I}$Zn-MFU-4 was analyzed using a Rietveld refinement with the occupancies of the peripheral Zn/Cu metal sites and capping Cl/H anions fixed based on the ICP-OES and $^{1}$H NMR results for the digested sample (Figure S10). Successful modeling of the bare framework was confirmed by analysis of the Fourier difference map, which does not show missing volumes of scattered intensity near the cluster. We also collected a powder synchrotron X-ray diffraction pattern for activated $Cu^{I}$Zn-MFU-4 for Rietveld refinement analysis, which yielded a structural model for the framework consistent with that obtained by neutron diffraction analysis (Figure S68). Based on the refined structure of the activated framework against the powder neutron

diffraction data collected at 1.5 K, the nearest $Cu^{I}\cdots Cu^{I}$ distance across the pore is 6.54(3) Å (Figure 4), whereas the nearest $Cu^{I}\cdots H$ and $Cu^{I}\cdots Cl$ distances are 5.87(3) and 5.63(3) Å, respectively. From the perspective of pore confinement, a neighboring Cl atom is located closer to the $Cu^{I}$ adsorption site and can exert stronger van der Waals interaction to influence the local environment experienced by adsorbed $H_2$. The probability that a $Cu^{I}$ site has at least one neighboring $M^{II}$–Cl (M = Zn, Cu) species at the adjacent clusters is ~40%, assuming a random distribution of peripheral species ($Cu^{I}$, $Cu^{II}$–Cl, $Zn^{II}$–H, and $Zn^{II}$–Cl) in the proposed chemical formula of $Cu_{1.6}Zn_{3.4}Cl_{0.6}H_{2.0}(bbta)_3$. Considering the van der Waals radii of each atom, the pore aperture surrounded by peripheral species is approximately 4–5 Å regardless of the identity of the peripheral species (Figure S69). This narrow pore offers a highly confining environment around the $Cu^{I}$ adsorption sites, consistent with the stronger $H_2$ adsorption enthalpy observed for $Cu^{I}$Zn-MFU-4 relative to the linker-expanded version, while still allowing diffusion of small gas molecules, as evidenced by gas adsorption analyses.

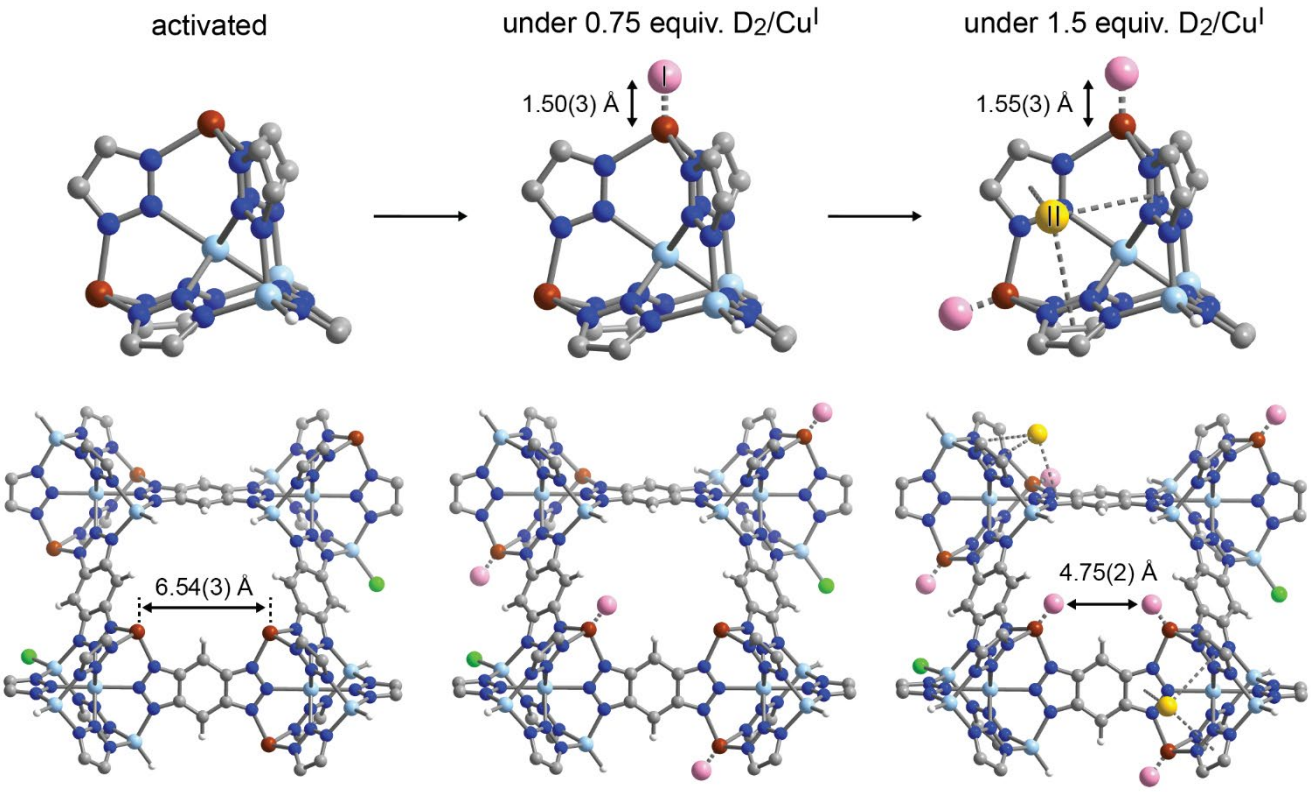


**Figure 4.** Structures of $Cu^{I}Zn$-MFU-4 under vacuum, with 0.75 equivalents of $D_2$ per $Cu^{I}$, and under 1.5 equivalents of $D_2$ per $Cu^{I}$, as obtained from Rietveld refinement against the powder neutron diffraction patterns. The top row highlights the pentanuclear cluster node, and the bottom row highlights one of the six faces of the cubic cage. Gray, blue, white, brown, light blue, and green spheres represent C, N, H, Cu, Zn, and Cl atoms, respectively. Pink and yellow spheres represent $D_2$ molecules modeled as super atoms at the first adsorption site (I) and the second adsorption site (II), respectively. The numbers of $D_2$ molecules and peripheral species ($Cu^{I}$, $Cu^{II}$–Cl, $Zn^{II}$–H, and $Zn^{II}$–Cl sites) illustrated in this figure have been adjusted to reflect their occupancies.

Using the structural model determined for the activated framework at 1.5 K as the initial structure, Rietveld refinement was performed against the diffraction pattern collected under 0.75

equivalents of $D_2$. The resulting crystal structure for $Cu^{I}$Zn-MFU-4 under 0.75 equivalents of $D_2$ per $Cu^{I}$ displays a Cu–$D_2$ distance of 1.50(3) Å measured from the Cu atom to the centroid of the $D_2$ molecule, represented by the super atom position, with an occupancy of $D_2$ within error of 0.75 equivalent of $D_2$ per $Cu^{I}$ (Figure 4). This Cu–$D_2$ distance is similar, within error, to that observed for $Cu^{I}$Zn-MFU-4*l* (1.53(2) Å) as determined by similar powder neutron diffraction experiments.[21] The comparable Cu–$D_2$ distance in these two frameworks is in good agreement with our previous computational study, which predicted that $Cu^{I}$–$H_2$ distances may only differ by ~0.04 Å even if the adsorption enthalpy varies by ~10 kJ/mol.[14,25]

The refined structure under 1.5 equivalents of $D_2$ loading revealed a Cu–$D_2$ distance of 1.55(3) Å, which falls within the error range of the substoichiometric $D_2$ loading measurement of 1.50(3) Å under 0.75 equivalents, with full occupancy at the $Cu^{I}$ site. The distance between each $D_2$ bound to $Cu^{I}$ across the pore was 4.75(2) Å (Figure 4), which is larger than the typical intermolecular separation in liquid $H_2$ (3.3–3.5 Å).[73] Therefore, an adsorbed $D_2$ (and $H_2$) molecule on one $Cu^{I}$ site minimally or negligibly impedes $D_2$ (and $H_2$) adsorption at nearby open metal sites. A second adsorption site was observed at the corner of the large pore, surrounded by three triazoles of the pentanuclear cluster (Figure 4). This adsorption site is analogous to that observed in an isoreticular framework $Cu^{I}$Mn-MFU-4*l* but with a shorter distance from the center of the triazole moiety (3.39(2) Å for $Cu^{I}$Zn-MFU-4 and 3.53(1) Å for $Cu^{I}$Mn-MFU-4*l*).[14] This secondary adsorption site is far from the $Cu^{I}$ sites, and therefore cannot interact with $D_2$ molecules at the $Cu^{I}$ sites. Rietveld refinement against the diffraction pattern collected under 2.5 equivalents of $D_2$ revealed a structure similar to that under 1.5 equivalents of $D_2$ with an increased occupancy for site II (Figure S62). Overall, the refined structures under excess $D_2$ indicate that each $Cu^{I}$ site and secondary adsorption sites likely behave independently for $D_2$ (and $H_2$) adsorption.

***In situ* Gas-Dosing Infrared Spectroscopy.** Examinations of vibrational and rotational modes of $H_2$ bound to a metal binding site provide insights into the degree of $H_2$ bond activation and therefore the strength of π-backbonding of the metal site.[14,50] Although the symmetric H–H vibration is infrared inactive in a free $H_2$ molecule, metal–$H_2$ interactions couple the H–H vibration with other modes, such as translation along the metal–$H_2$ bond, inducing a change in the dipole moment and making it infrared active.[45,50] We collected *in situ* $H_2$- and $D_2$-dosed infrared spectra on $Cu^{I}$Zn-MFU-4 to investigate the H–H and D–D stretching vibration upon adsorption. Spectra were recorded under ~600 mbar of $H_2$ or $D_2$ at 90 K, and a difference spectrum was created by subtracting the $D_2$-dosed spectrum from the $H_2$-dosed spectrum to isolate the signals arising from the adsorbed species (Figure 5a). Generating a difference spectrum is essential because vibrational signals related to $Cu^{I}$ and linkers are noticeably perturbed upon gas binding. The assignments of adsorbed species are difficult without canceling these effects by conducting measurements using the isotopically labeled gas.

The difference spectra for $H_2$- and $D_2$-dosed $Cu^{I}$Zn-MFU-4 revealed a broad asymmetric signal of adsorbed $H_2$ with a peak maximum at ~3270 $cm^{-1}$ and a sharper peak at ~4120 $cm^{-1}$ (Figure 5a). The broad asymmetric peak is characteristic of the H–H stretching mode ($\nu$(H–H)) of $H_2$ that is strongly bound to $Cu^{I}$ sites, while the sharp peak arises from weakly physisorbed $H_2$. The signals for adsorbed $D_2$ in $Cu^{I}$Zn-MFU-4 were observed at ~2344 $cm^{-1}$ and ~2970 $cm^{-1}$ for strongly bound $Cu^{I}$ sites and nonmetal physisorption sites, respectively. The isotope shift for each adsorption site closely matches the expected change based on the reduced mass of $H_2$ and $D_2$ under a simple harmonic oscillator approximation, corroborating the assignment (for physisorption sites 4120:2970 ≈ 1.39:1 while for $H_2$ at $Cu^{I}$ sites 3270:2344 ≈ 1.40:1; the expected ratio is 1.41:1).

Given the $\nu$(H–H) frequency of bulk $H_2$ (4161 $cm^{-1}$),[74] the $\nu$(H–H) frequency of 3270 $cm^{-1}$ for the $H_2$ molecule at a $Cu^I$ site suggests a weakened H–H bond via π-backbonding interactions. This stretching band for $Cu^I$Zn-MFU-4 is ~20 $cm^{-1}$ higher compared to $Cu^I$Zn-MFU-4*l*, indicating that the H–H bond observed in $Cu^I$Zn-MFU-4 is less activated through π-backbonding. Nevertheless, when comparing the $\nu$(H–H) position across a series of $Cu^I$M-MFU-4*l* (M = Zn, Mn, Cd) and $Cu^I$Zn-MFU-4, the $\nu$(H–H) frequency in $Cu^I$Zn-MFU-4 is closest to that in $Cu^I$Zn-MFU-4*l* (Table 2). The weaker π-backbonding in $Cu^I$Zn-MFU-4 compared to $Cu^I$Zn-MFU-4*l* does not necessarily contradict the stronger $\Delta H_{ads}$ observed in gas adsorption study, due to the amphoteric nature of the $H_2$ molecule, which can act as a σ-donor and a π-acceptor. Indeed, some molecular $H_2$ complexes with strong $H_2$ binding exhibit a smaller shift in $\nu$(H–H) than those with weaker $H_2$ binding, due to differences in σ-interactions.[75] The D–D stretching ($\nu$(D–D)) peak in $Cu^I$Zn-MFU-4 appeared at a marginally smaller wavenumber by ~10 $cm^{-1}$. However, because this observed difference is close to the resolution of the spectra (4 $cm^{-1}$), we elected not to discuss the trend for $D_2$ in detail.

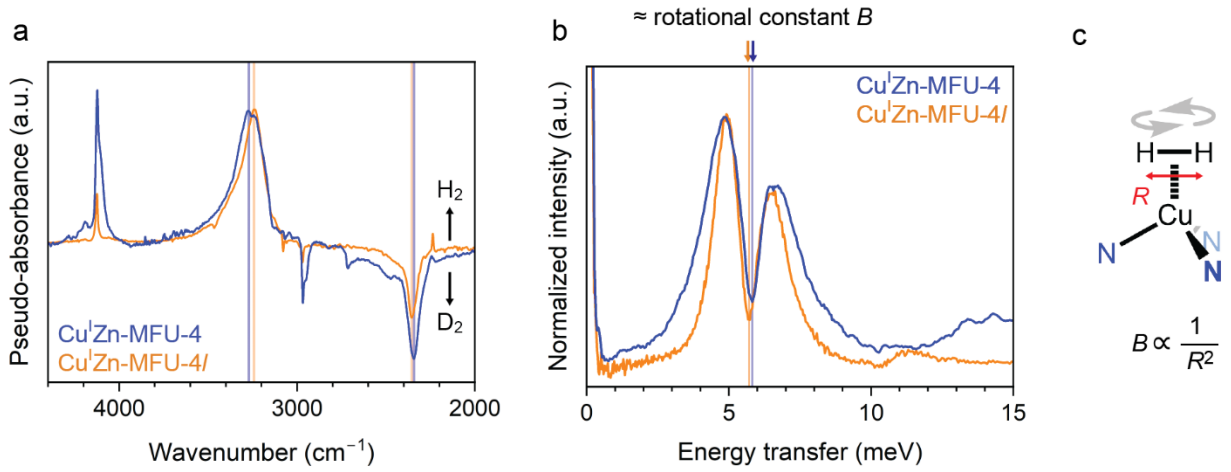


**Figure 5.** (a) *In situ* $H_2$- and $D_2$-dosed infrared spectra collected at 90 K for $Cu^I$Zn-MFU-4 (blue) and $Cu^I$Zn-MFU-4*l* (orange),[14] where the $D_2$-dosed spectrum was subtracted from the $H_2$-dosed spectrum. The signals corresponding to $H_2$ and $D_2$ appear as positive and negative peaks, respectively. The blue and orange vertical lines represent the peak maximum for $H_2$ and $D_2$ bound

to $Cu^I$ sites in $Cu^I$Zn-MFU-4 and $Cu^I$Zn-MFU-4*l*, respectively. (b) *In situ para*-$H_2$-dosed inelastic neutron scattering spectra for $Cu^I$Zn-MFU-4 (blue) and $Cu^I$Zn-MFU-4*l* (orange)[46] from 0 to 15 meV. The spectrum of an activated framework was subtracted from the gas-dosed spectrum to isolate signals from $H_2$. The vertical lines represent the splitting center, which is approximated to the rotational constant *B* of an $H_2$ molecule bound to $Cu^I$ under the quasi-two-dimensional rotor model. (c) The relationship between the H–H distance and the rotational constant of an $H_2$ molecule.

**Table 2. Summary of H–H Stretching Peak of $H_2$ Bound to a $Cu^I$ Site**

| material | *v*(H–H) ($cm^{-1}$) | | | full width at half maximum ($cm^{-1}$) | |
|---|---|---|---|---|---|
| | observed[a] | calcd. for cluster model[b] | calcd. by MD[c] | observed | calcd. by MD[c] |
| $Cu^I$Zn-MFU-4 | 3270 | 3425 | 3350 | 190 | 167 |
| $Cu^I$Zn-MFU-4*l* | 3250 | 3420 | 3340 | 150 | 157 |
| $Cu^I$Mn-MFU-4*l*[14] | 3300 | | | 130 | |
| $Cu^I$Cd-MFU-4*l*[14] | 3380 | | | 110 | |

[a]At 90 K. [b]Obtained by DFT calculations for pentanuclear cluster models with the ωB97X-D4/Basis-1 level theory. [c]Obtained by molecular dynamics simulations using periodic boundary conditions.

While the positions of the peak maximum for *v*(H–H) at $Cu^I$ sites were similar between $Cu^I$Zn-MFU-4 and $Cu^I$Zn-MFU-4*l*, the peak width for *v*(H–H) at $Cu^I$ sites is noticeably broader for $Cu^I$Zn-MFU-4 (Table 2). We also observed a trend in the peak width for *v*(H–H) across $Cu^I$M-MFU-4*l* (M = Zn, Mn, Cd) frameworks, in which the *v*(H–H) peak becomes broader for a framework that strongly binds $H_2$ (Table 2).[14] The observations in gas-dosed infrared spectra (both peak positions and widths) will be revisited in the computational sections with cluster model calculations and molecular dynamics simulations.

**Inelastic Neutron Scattering Measurements.** To further understand the dynamics and potential energy surface of the $H_2$ molecule bound to $Cu^I$, inelastic neutron scattering (INS) spectra were recorded for both the activated framework and the framework under 0.75 equivalents of *para*-$H_2$ at 5 K (Figure 5b). Inelastic neutron scattering measurements probe quantum rotational transitions of the $H_2$ molecule at low energy transfer values, offering information about electronic interactions between the $H_2$ and the metal site, and steric effects through the rotational constant and the barrier to rotation.[14,46,76] We employed a simplified model of a quasi-two-dimensional rotor to compare the inelastic neutron scattering results of $Cu^I$Zn-MFU-4 with the previous studies on $Cu^I$Zn-MFU-4*l*.[46]

In brief, a quasi-two-dimensional rotor model has the center of the $H_2$ molecule on the $C_3$ axis (*z* axis) of the $C_{3v}$-symmetric trigonal Cu site and allows the $H_2$ molecule to rotate about the azimuthal angle within the plane perpendicular to the $C_3$ axis. The potential profile of a quasi-two-dimensional rotor model predicts that the lowest excitation energy levels, $(J, M_J) = (1, \pm1)$, which are originally degenerate in an isotropic environment, will split due to the directional requirement for π-backbonding interactions with the $Cu^I$ site. According to this simplified model, the degree of the splitting increases as the in-plane anisotropy of the potential energy surface increases, while the center of splitting can be approximated to the rotational constant *B*. Despite the simplification compared to the three-dimensional landscape in real space, this model has been successful in capturing the trend in π-backbonding strength through the estimated rotational constant *B* for $Cu^I$Zn-MFU-4*l* and $Cu^I$Mn-MFU-4*l* in our previous study.[14] Here, we aim to compare qualitatively the potential energy surface of $H_2$ rotation between $Cu^I$Zn-MFU-4 and $Cu^I$Zn-MFU-4*l*.

The inelastic neutron scattering spectrum of $Cu^I$Zn-MFU-4 dosed with 0.75 equivalents of *para*-$H_2$, subtracted with that of the bare framework collected at 5 K, features doubly split peaks at 4.87

and 6.62 meV (Figure 5b). We assign these peaks to rotational excitations of *para*-$H_2$ from the $J = 0$ to $J = 1$ states. The center of the splitting was 5.8 meV, which can be approximated to the rotational constant $B$ of the $H_2$ molecule in the quasi-two-dimensional rotor model. Because the $B$ value for a diatomic molecule is inversely proportional to the square of the bond distance under a rigid rotor approximation (Figure 5c), the estimated rotational constant $B$ of 5.8 meV suggests an H–H distance ($d$(H–H)) of 0.85 Å for $H_2$ bound to $Cu^{I}$Zn-MFU-4. This $d$(H–H) value is longer than that in free $H_2$, which is 0.74 Å with $B = 7.54$ meV, indicating that the H–H bond elongates via π-backbonding at $Cu^{I}$ sites in $Cu^{I}$Zn-MFU-4.

We next compared the inelastic neutron scattering spectrum of *para*-$H_2$-dosed $Cu^{I}$Zn-MFU-4 with that reported for $Cu^{I}$Zn-MFU-4*l* (Figure 5b).[46] Although inelastic neutron scattering spectra under *para*-$H_2$ are almost overlapping for $Cu^{I}$Zn-MFU-4 and $Cu^{I}$Zn-MFU-4*l* in the region for the rotational excitations of *para*-$H_2$ from the $J = 0$ to $J = 1$ states, closer inspection reveals that the center of splitting is located at a slightly higher energy by ~0.1 meV, implying a slightly larger $B$ for $Cu^{I}$Zn-MFU-4. The slight shift in the position of the splitting center to higher energy for $Cu^{I}$Zn-MFU-4 could correspond to a shorter H–H distance for the $H_2$ molecule bound to the $Cu^{I}$ sites, suggesting less H–H activation. Although the resolution of the spectra (~0.09 meV) prohibits interpretation of the data based on the subtle shift observed (~0.1 meV), the comparable or only slightly weaker H–H activation in $Cu^{I}$Zn-MFU-4 aligns with the slightly larger H–H stretching frequency observed by *in situ* gas-dosing infrared spectroscopy.

While the peak splitting center of the doublet for rotational excitations from the $J = 0$ to $J = 1$ states relates to the rotational constant $B$ in a quasi-two-dimensional rotor model, the gap of splitting is associated with the anisotropy of the potential surface along the rotation axis. The splitting gap appears wider in $Cu^{I}$Zn-MFU-4 compared to that in $Cu^{I}$Zn-MFU-4*l*, suggesting a

more anisotropic potential energy surface in $Cu^{I}$Zn-MFU-4 along the $Cu^{I}$–$H_2$ axis under the quasi-two-dimensional rotor model because π-backbonding interactions are directionally dependent. The larger anisotropy of the potential surface of $H_2$ rotation in $Cu^{I}$Zn-MFU-4 could arise from its stronger $H_2$ binding than that of $Cu^{I}$Zn-MFU-4*l*.

In addition to a larger gap in the splitting, we observe that each peak is broader for $Cu^{I}$Zn-MFU-4. This broadening could originate from heterogeneity in pore environments caused by the partial Cu and anion exchange. Although $Cu^{I}$Zn-MFU-4*l* also exhibits partial $Cu^{I}$ occupancy to have a heterogeneous pore environment, its larger pore size spaces each pentanuclear cluster node ~11 Å apart. This increased separation reduces the influence of neighboring cluster compositions on the potential energy surface for $H_2$ binding around $Cu^{I}$ at each cluster node. Conversely, in ultramicroporous $Cu^{I}$Zn-MFU-4, the distance between a $Cu^{I}$ site and other peripheral species (Zn–H, Zn–Cl, $Cu^{II}$–Cl, or $Cu^{I}$) in adjacent clusters can be as short as ~6.5 Å (Figure 4). This short cluster–cluster distance may affect the potential energy well for $H_2$ at $Cu^{I}$ sites, depending on the neighboring cluster composition. The discussion on the peak width could also be applied to interpret the width of the H–H stretching peak observed in infrared spectroscopy. Such broadening of vibrational and rotational modes represents an additional indicator of pore confinement in $Cu^{I}$Zn-MFU-4, alongside the enhancement of adsorption enthalpy.

***In situ* $H_2$-Dosing L-edge X-Ray Absorption Spectroscopy.** Previously, *in situ* gas-dosing Cu L-edge X-ray absorption spectroscopy was employed for elucidating metal–gas interactions in $Cu^{I}$Zn-MFU-4*l*.[77] Metal L-edge X-ray absorption spectroscopy can probe dipole-allowed excitations of a core-level 2p electron to 3d holes, as opposed to the weaker dipole-forbidden transitions of a 1s electron to 3d holes probed by metal K-edge X-ray absorption spectroscopy. In the case of $Cu^{I}$ with a formally filled $d^{10}$ configuration, *in situ* gas-dosing Cu L-edge X-ray

absorption spectroscopy can probe unoccupied antibonding orbitals between Cu and the adsorbed molecule with Cu 3d character (Figure 6a).[21,77]

We performed *in situ* $H_2$-dosing Cu L-edge X-ray absorption spectroscopic measurements on $Cu^{I}$Zn-MFU-4 to compare the energy of these transitions with those of $Cu^{I}$Zn-MFU-4*l*, aiming to understand the electronic differences in orbital interactions caused by $H_2$ binding between the two frameworks. The spectrum for $Cu^{I}$Zn-MFU-4 under vacuum reveals a broad edge feature that is most intense at 935 eV, with a minor pre-edge feature at 931 eV (Figure 6b). The pre-edge feature in the L-edge spectrum was also observed for $Cu^{I}$Zn-MFU-4*l*, which was synthesized using a procedure similar to $Cu^{I}$Zn-MFU-4 (i.e., $Cu^{II}$-exchange and formate-exchange followed by autoreduction of $Cu^{II}$–$O_2CH$), and was attributed to a small amount of residual $Cu^{II}$ species resulting from incomplete formate-exchange or trace $Cu^{II}$ defects.[77,78] The main edge feature could result from excitations to empty antibonding orbitals between Cu 3d orbitals and π-systems of the linkers.[77,79]

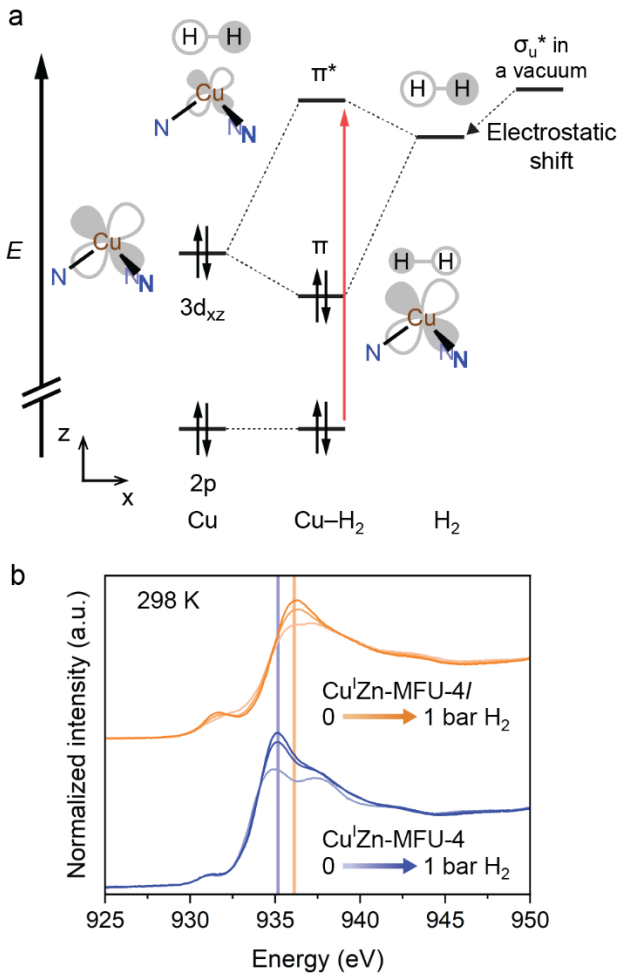


**Figure 6.** (a) A simplified molecular orbital diagram showing interactions between $Cu^I$ and $H_2$ with cartoon representations of the resultant molecular orbitals as a linear combination of atomic orbitals. The degenerate $3d_{yz}$ orbital is omitted for clarity. The $\sigma_u^*$ orbital of a free $H_2$ molecule is lowered in energy when the molecule approaches $Cu^I$ by the positive charge. The red arrow illustrates the transition observed in Cu L-edge X-ray absorption spectra for $Cu^I$Zn-MFU-4 and $Cu^I$Zn-MFU-4*l* dosed with $H_2$. (b) *In situ* $H_2$-dosed Cu L-edge X-ray absorption spectra for $Cu^I$Zn-MFU-4*l* (orange)[77] and $Cu^I$Zn-MFU-4 (blue).

Upon $H_2$ dosing to $Cu^I$Zn-MFU-4 at 298 K, a new spectral feature appears at 935.2 eV, which is ~1 eV lower in energy than that corresponding peak at 936.3 eV in the $H_2$-dosed spectra of $Cu^I$Zn-MFU-4*l* (Figure 6b). In both cases, we assign the new feature to an excitation into the π* orbital between Cu and $H_2$. In our prior study of $Cu^I$Zn-MFU-4*l*,[77] we determined that the energy of this feature depends on several factors, including the 2p core level energy for the $Cu^I$ sites, and the strength of the π-backbonding interaction between the $Cu^I$ sites and $H_2$, which is related to the energy gap between the $Cu^I$ 3d shell and the $\sigma_u$* orbital of the $H_2$ molecule. The lower energy of the 2p-to-π* feature in the $H_2$-dosed $Cu^I$Zn-MFU-4 spectrum compared to that in the $Cu^I$Zn-MFU-4*l* spectrum indicates a lower energy level for the π* orbital between Cu and $H_2$ and/or a higher energy level for 2p core orbital. Of these possibilities, we expect that the former explanation—the energy level of the π* orbital of $Cu^I$Zn-MFU-4 is lower than that of $Cu^I$Zn-MFU-4*l*—is more reasonable. The electron-deficient $bbta^{2-}$ linker in $Cu^I$Zn-MFU-4 should increase the effective nuclear energy of the metal to lower the energy of the Cu 3d orbitals, and to a lesser extent the $\sigma_u$* orbital of $H_2$ through electrostatic interaction with $Cu^I$ (Figure 6a).[77] The net result should be to widen the energy gap between the Cu 3d orbitals and the $H_2$ $\sigma_u$* orbital for $Cu^I$Zn-MFU-4 compared to the gap for $Cu^I$Zn-MFU-4*l*, leading to a weaker π-backbonding interaction and a lower energy for the π* orbital. This explanation is corroborated by the vibrational and rotational spectra that indicate weaker π-backbonding interactions in $Cu^I$Zn-MFU-4.

The second possibility to explain the lower energy for the 2p-to-π* feature—the Cu 2p core levels are higher in energy for $Cu^I$Zn-MFU-4 than for $Cu^I$Zn-MFU-4*l*—is unlikely. The energy of the Cu core 2p electrons in $Cu^I$Zn-MFU-4 should instead be lower than in $Cu^I$Zn-MFU-4 due to the more electron-deficient $bbta^{2-}$ linker, consistent with the stabilization of the Cu 3d orbitals as discussed above. We expect that the stabilization of the 2p core level is less than the lowering shift

of the π* orbital, leading to an overall lower energy for the 2p-to-π* transition for $H_2$-dosed $Cu^I$Zn-MFU-4.

Note that, although L-edge peak intensity is often used to gauge the degree of d character in an unoccupied orbital to which the L-edge transition takes place, thereby probing the strength of π-backbonding interactions,[80,81] partial $H_2$ coverage at $Cu^I$ sites at 1 bar and 298 K for these $Cu^I$Zn-MFU-4 and $Cu^I$Zn-MFU-4*l* frameworks precludes direct comparison of the peak intensities.

**Computational Analysis.** To further understand the origins of the differences in $H_2$ adsorption at $Cu^I$ sites in $Cu^I$Zn-MFU-4 and $Cu^I$Zn-MFU-4*l*, density functional theory (DFT) calculations were performed using a truncated cluster model of the pentanuclear secondary building unit. Previous computational studies using similar pentanuclear cluster models have successfully replicated the experimentally observed trends in $H_2$ adsorption enthalpies across the $Cu^I$M-MFU-4*l* (M = Zn, Mn, Cd) series, with different M metal centers at the core of the pentanuclear cluster node.[14,25] In the present study, we focus on understanding how the identity of the triazolate linker affects $H_2$ binding. To do this, we constructed two pentanuclear cluster models with one peripheral open $Cu^I$ site. One model features the $Cu^I$ site surrounded by partially protonated $bbta^{2-}$ linkers and the other features the $Cu^I$ site surrounded by 5,6-dihydroxybenzotriazolate ($dhbta^-$), representing $Cu^I$Zn-MFU-4 and $Cu^I$Zn-MFU-4*l*, respectively. Benzotriazolate ligands farther from the $Cu^I$ site are truncated to retain only a 1,2,3-triazolate fragment ($ta^-$) for computational efficiency. The resulting cluster compositions are $CuZn_4Cl_3(Hbbta)_3(ta)_3$ and $CuZn_4Cl_3(dhbta)_3(ta)_3$ for $Cu^I$Zn-MFU-4 and $Cu^I$Zn-MFU-4*l*, respectively (Figure 7a).

The geometry optimization of the cluster models with $H_2$ bound at the $Cu^I$ site was performed using the ωB97X-D4 functional with the def2-TZVPP basis on Cu and $H_2$, and the def2-SVPD basis on all other atoms (denoted as Basis-1 hereafter, see details in the SI).[82,83] In both models,

the $H_2$ molecule binds side-on at the same distance between $Cu^I$ and the centroid of $H_2$ ($d$(Cu–$H_2$) = 1.659 Å; Figure 7a). The H–H distance ($d$(H–H)) is elongated by ~0.05 Å compared to free $H_2$ due to π-backbonding in both models, with just a 0.001 Å difference between the two models (0.793 Å for the $Cu^I$Zn-MFU-4 model and 0.794 Å for the $Cu^I$Zn-MFU-4*l* model). The almost identical and only slightly shorter $d$(H–H) in the $Cu^I$Zn-MFU-4 and $Cu^I$Zn-MFU-4*l* model clusters align with the results from *in situ* $H_2$-dosing inelastic neutron scattering spectroscopy.

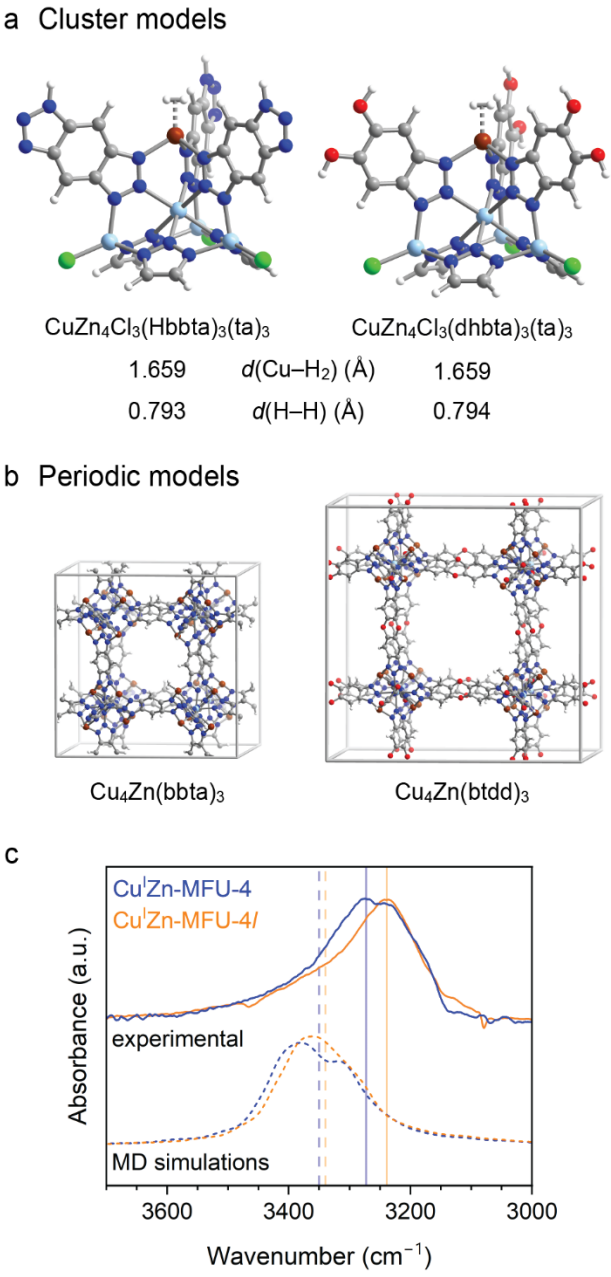


**Figure 7.** (a) Optimized structures of cluster models for Cu$^{I}$Zn-MFU-4 and Cu$^{I}$Zn-MFU-4*l* with an adsorbed $H_2$ molecule using DFT. (b) A snapshot of molecular dynamics (MD) simulations for $H_2$ binding in periodic boundary models of Cu$^{I}$Zn-MFU-4 and Cu$^{I}$Zn-MFU-4*l*. (c) Experimental (solid line; a magnified view of Figure 5a) and simulated (broken line) vibrational spectra for the H–H stretching mode of an $H_2$ molecule bound to Cu$^{I}$Zn-MFU-4 (blue) and Cu$^{I}$Zn-MFU-4*l*

(orange). Solid vertical lines represent the wavenumber at the peak maximum for each experimental spectrum, and the broken vertical lines represent the weighted average of the vibrational frequencies obtained from the MD simulations. Atom colors: gray, blue, red, white, brown, light blue, and green spheres represent C, N, O, H, Cu, Zn, and Cl, respectively.

The estimated $H_2$ adsorption enthalpies for these models ($\Delta H°_{DFT}$) are −29.3 kJ/mol and −28.2 kJ/mol for $Cu^{I}$Zn-MFU-4 and $Cu^{I}$Zn-MFU-4*l*, respectively (Table 3). The cluster models thus successfully capture the trend that $Cu^{I}$Zn-MFU-4 adsorbs $H_2$ more strongly than $Cu^{I}$Zn-MFU-4*l*. This trend remains unchanged regardless of the density functional employed (Table S20), confirming that the linker identity measurably affects the $Cu^{I}$–$H_2$ binding energy at the pentanuclear cluster node. However, we note that the difference in $\Delta H°_{DFT}$ between the two cluster models is smaller than that in the isosteric enthalpy of adsorption obtained via the Clausius–Clapeyron method ($\Delta H_{ads}$). These cluster-based calculations do not include pore confinement effects,[32] which are expected to further influence adsorption behavior and could enhance $H_2$ adsorption in $Cu^{I}$Zn-MFU-4. Therefore, pore confinement may explain the larger difference in experimentally measured $\Delta H_{ads}$ between $Cu^{I}$Zn-MFU-4 and $Cu^{I}$Zn-MFU-4*l* (as determined by the Clausius–Clapeyron analysis) compared to the predictions from the cluster models.

Given the insensitivity of $H_2$ adsorption enthalpies upon the first coordination sphere of the metal site,[63] the 1 kJ/mol difference between the two cluster models remains significant. To understand the reason for the increased $H_2$ binding strength when changing the ligand observed in these cluster model calculations, we performed energy decomposition analyses based on absolutely localized molecular orbitals (ALMO-EDA).[84–86]

Among different interaction components, the frozen interaction energy term $\Delta E_{Frz}$ (which includes electrostatic interactions, dispersion, and Pauli repulsion) showed a lower energetic penalty for the $Cu^{I}$Zn-MFU-4 model compared to the $Cu^{I}$Zn-MFU-4*l* model (Table 3). The reduction in $\Delta E_{Frz}$ can be attributed to the more positively charged $Cu^{I}$ site in $Cu^{I}$Zn-MFU-4, which results from the presence of a more electron-withdrawing triazolate functional group on the benzotriazolate ligand. The amount of charge transferred from $Cu^{I}$ to $H_2$ in terms of electrons is smaller for the $Cu^{I}$Zn-MFU-4 model, suggesting weaker π-backbonding, consistent with spectroscopic experiments. Although the amount of charge transfer by π-backbonding is smaller, the charge transfer energy term ($\Delta E_{CT}$) is slightly more favorable for the $Cu^{I}$Zn-MFU-4 model. This observation indicates that the decrease in π-backbonding from $Cu^{I}$ to $H_2$ is offset by the more favorable σ-donation from $H_2$ to $Cu^{I}$. Overall, the cluster model calculations indicate that the stronger $H_2$ binding in $Cu^{I}$Zn-MFU-4 may partly result from the more positively charged $Cu^{I}$ site, which outcompetes reduced π-backbonding. This balancing effect between σ-donation and π-backbonding, as reflected in changes in charge density at the trigonal $Cu^{I}$ site, illustrates the amphoteric nature of $H_2$ as a ligand.[87] We note that the additional increase in adsorption enthalpy for $Cu^{I}$Zn-MFU-4 relative to $Cu^{I}$Zn-MFU-4*l* absent in the cluster models could be due to pore confinement effects that are challenging to model.

**Table 3. Enthalpy of Adsorption Calculation and Energy Decomposition Analysis Results from Application of the ALMO-EDA Method to Pentanuclear Cluster Models at the ωB97M-V/Basis-1 Level**

| material | $Cu^{I}$Zn-MFU-4 | $Cu^{I}$Zn-MFU-4*l* |
|---|---|---|
| cluster model | $CuZn_4Cl_3(Hbbta)_3(ta)_3$ | $CuZn_4Cl_3(dhbta)_3(ta)_3$ |
| energy contribution (kJ/mol) | | |

| | | |
|---|---|---|
| $\Delta E_{prep}$[a] | 15.6 | 15.9 |
| $\Delta E_{frz}$[b] | 43.0 | 44.2 |
| $\Delta E_{pol}$[c] | −49.3 | −49.8 |
| $\Delta E_{CT}$[d] | −46.2 | −46.0 |
| $\Delta E_{total}$ | −36.9 | −35.7 |
| enthalpy of adsorption (kJ/mol) | | |
| $\Delta H°_{DFT}$ | −29.3 | −28.2 |
| charge transfer (atomic units) | | |
| $Cu^I$ to $H_2$ | 0.0242 | 0.0246 |

[a]Energy required to distort each fragment to the geometry in the bonded state. [b]Energy change arising without relaxation of the fragment orbitals, which includes interfragment electrostatics, Pauli repulsion, and dispersion interactions. [c]Energy arising from relaxation of self-contained fragment orbitals in the presence of the field of the other fragment. [d]Stabilization energy by charge transfer between the fragments.

The calculated vibrational frequency for the H–H stretch (ν(H–H)) in the $Cu^I$Zn-MFU-4 cluster model is higher—corresponding to a less activated H–H bond—than that for the $Cu^I$Zn-MFU-4*l* cluster model (Table 2), which agrees with the trend observed experimentally. However, the difference in vibrational frequencies between these models, based on static harmonic calculations with anharmonic corrections, was only 5 $cm^{-1}$, which is less than the experimental difference of ~20 $cm^{-1}$.

To better understand the vibrational dynamics of the adsorbed $H_2$ molecules, we conducted molecular dynamics (MD) simulations using periodic boundary conditions. The unit cell for molecular simulations includes eight pentanuclear cluster nodes in both frameworks, with $Cu^I$ sites placed at all four peripheral sites of each cluster to simplify the periodic model (Figure 7b; see the SI for other technical details). We expect that MD calculations can capture the probability density distributions of H–H bond lengths and their coupling with lower-frequency vibration modes, providing more detailed insights into both vibrational frequencies and peak broadening.

Simulated spectra derived from molecular dynamics revealed a larger difference of 10 $cm^{-1}$ in the weighted average of ν(H–H) between $Cu^{I}$Zn-MFU-4 and $Cu^{I}$Zn-MFU-4*l*, which is closer to the difference observed experimentally (Figure 7c). Addressing the shape of the *ν*(H–H) peaks for $H_2$ molecules bound to $Cu^{I}$ sites, the $Cu^{I}$Zn-MFU-4 framework exhibited a broader band than that in the $Cu^{I}$Zn-MFU-4*l* framework both experimentally and computationally, as indicated by the full width at half maximum (Table 2). Specifically, the ν(H–H) peak is distributed more to the higher-wavenumber side for $Cu^{I}$Zn-MFU-4, while the peak profile on the lower-wavenumber side overlaps almost completely for both frameworks. A similar trend—peak shift to higher wavenumbers and peak broadening—was also observed for MD simulations with $D_2$ (Figure S70).

The broadening of the *ν*(H–H) (and *ν*(D–D)) peak could result from several factors, including: (1) the dependency of the *ν*(H–H) frequency with respect to the $Cu^{I}$–$H_2$ distance,[46] (2) coupling with lower-frequency vibration modes such as the center-of-mass translations[46,47] and rotation[88] of $H_2$ ($D_2$), and (3) the heterogeneity of the pore environment around $Cu^{I}$ sites due to the partial metal-exchange and ligand exchange. To elaborate further on the first point, the $Cu^{I}$–$H_2$ distance has a probability density distribution.[46] While the $Cu^{I}$–$H_2$ distance cannot be shorter than the sum of atomic radii of the atoms, the probability density distribution of the $Cu^{I}$–$H_2$ distance could be extended toward the longer $Cu^{I}$–$H_2$ distance side for $Cu^{I}$Zn-MFU-4 due to stronger $H_2$ adsorption. Because π-backbonding strength depends on the $Cu^{I}$–$H_2$ distance, the difference in the probability density distribution of the $Cu^{I}$–$H_2$ distance between two frameworks leads to the broadening of the *ν*(H–H) signal at a higher frequency side for $Cu^{I}$Zn-MFU-4, as observed experimentally and computationally. Regarding the second point, the broadening of the ν(H–H) peak in $Cu^{I}$Zn-MFU-4 could arise from enhanced coupling between ν(H–H) and lower-frequency modes, enabled by the reduced π-backbonding character of the $Cu^{I}$–$H_2$ interaction. Because π-backbonding typically

favors a more directional interaction, its reduction in $Cu^{I}$Zn-MFU-4 may allow greater vibrational freedom and stronger coupling with the framework lattice modes, leading to the observed spectral features. The third point, heterogeneity of the pore environment around $Cu^{I}$ sites, was discussed earlier when considering the inelastic neutron scattering (INS) spectra. We note that, because the MD simulations were performed for periodic models that have four $Cu^{I}$ per pentanuclear cluster to create a homogeneous pore environment, this heterogeneity point is applicable only to experimental spectra and the broadening in the simulated spectra are explained solely by the first and second points.

**Investigation of HD and $D_2$ Adsorption for Hydrogen Isotope Separations.** In the previous sections, we examined fundamental differences in $H_2$ adsorption properties between $Cu^{I}$Zn-MFU-4 and $Cu^{I}$Zn-MFU-4*l* to understand the reason for the stronger $H_2$ adsorption in $Cu^{I}$Zn-MFU-4. We then sought a potential application of the strongest $H_2$ adsorption in $Cu^{I}$Zn-MFU-4 among the reported porous adsorbents. Because $H_2$ adsorption at the $Cu^{I}$ sites in $Cu^{I}$Zn-MFU-4 is strong enough, while still being reversible, to approach saturation even at 1 bar and 298 K, the material could be suitable for an isothermal pressure swing separation process. Of particular significance from energy and cost perspectives, this might even be viable at 298 K swinging between adsorption at 1 bar (with no compression) and desorption near 0.1 bar (enabling use of industrial-grade vacuum).[89,90]

We therefore elected to examine the possibility of ambient-temperature hydrogen isotope separations using $Cu^{I}$Zn-MFU-4. Our expectation is that thermodynamic selectivity for the heavier isotopic molecules (HD and $D_2$) will arise from differences in the zero-point energies of the vibrational modes associated with the metal–gas bond. Such effects are known as equilibrium isotope effects[91,92] for molecular hydrogen complexes[50,51,56] and can enable what is referred to as

chemical affinity quantum sieving (CAQS) for porous adsorbents.[49] In addition to $Cu^{I}$Zn-MFU-4, we analyzed $Cu^{I}$Zn-MFU-4*l* for HD and $D_2$ adsorption, as this material was previously identified as one of the top-performers for $D_2/H_2$ separations at cryogenic temperatures.[46,47] Significantly, the stronger $H_2$ adsorption in $Cu^{I}$Zn-MFU-4 is expected to lead to a larger $D_2/H_2$ selectivity relative to $Cu^{I}$Zn-MFU-4*l* and potentially allow separations to be practical at room temperature.

Adsorption isotherms of hydrogen deuteride (HD) and dideuterium ($D_2$) were collected near ambient temperature (5–45 °C; 278–318 K) for $Cu^{I}$Zn-MFU-4 and $Cu^{I}$Zn-MFU-4*l*. Notably, although the adsorption isotherm profiles of the isotopic gases are similar, the initial slopes of the isotherms for heavier isotopic gas molecules were distinctly steeper for both $Cu^{I}$Zn-MFU-4 and $Cu^{I}$Zn-MFU-4*l* (Figures 8a and S39), with the expected trend of gas uptake following $D_2$ > HD > $H_2$.[93] We note that the difference in uptake between these gases in $Cu^{I}$Zn-MFU-4 is smaller above 1 bar than at lower pressures, because the isotherm profiles level off near 1 bar, approaching the saturation of the $Cu^{I}$ sites at these temperatures. Instead of focusing solely on the uptake value at a specific condition from a single-component isotherm, we need to consider binding strength to better understand selectivity.

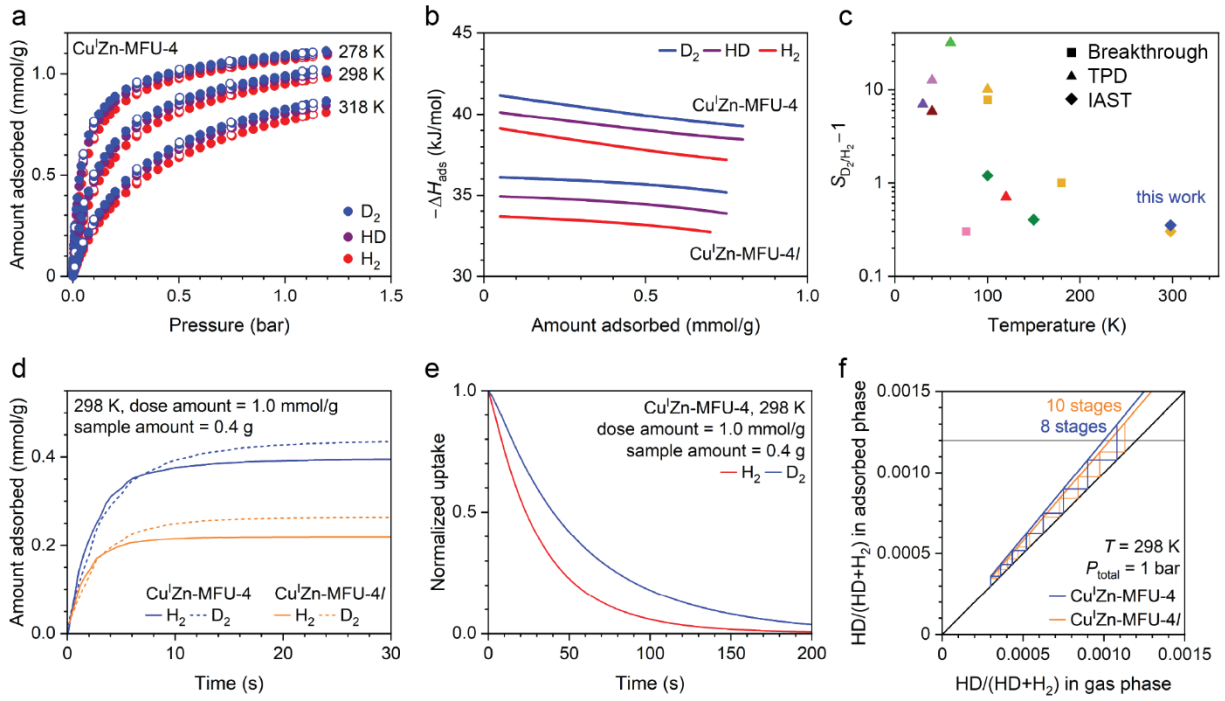


**Figure 8.** (a) Adsorption isotherms of hydrogen isotopes ($D_2$, HD, and $H_2$) for $Cu^{I}$Zn-MFU-4 collected at 278, 298, and 318 K (see Figure S32 for data collected at 288 and 308 K). Filled and open circles represent adsorption and desorption data, respectively. (b) Isosteric enthalpies of adsorption for $D_2$, HD, and $H_2$ in $Cu^{I}$Zn-MFU-4 and $Cu^{I}$Zn-MFU-4*l* estimated using the Clausius–Clapeyron method with adsorption isotherms from 278 to 318 K. (c) Summary of $D_2/H_2$ selectivity with respect to temperature in selected porous adsorbents: $Mn(ta)_2$ (light green),[94] MIL-53(Al) (pale purple),[95] Cocryst1 (6ET-RCC3-*R*/CC3-*S*; purple),[44] ZnCl-MFU-4 (brown),[43] $Ni_2$(dobdc) (green),[56] Cu-ZIF-gis (red),[96] zeolite 13X (pink),[97] $Cu^{I}$Zn-MFU-4*l* (yellow),[46,47] and $Cu^{I}$Zn-MFU-4 (blue). Symbols denote different methods for determining $D_2/H_2$ selectivity, with squares, triangles, and diamonds representing selectivities determined by breakthrough experiments, temperature programmed desorption (TPD) analyses, and ideal adsorbed solution theory (IAST) based on single-component adsorption isotherms. (d–e) Single-component adsorption (d) and desorption (e) kinetics data with $H_2$ and $D_2$ for $Cu^{I}$Zn-MFU-4 and $Cu^{I}$Zn-MFU-4*l*. (f) McCabe–

Thiele analyses to assess the theoretical number of equilibrium stages required to enrich HD from natural abundance (0.015 mol D%; $HD/H_2$ = 0.0003/99.9997) by four-fold (the horizontal gray line) using $Cu^{I}Zn$-MFU-4 (blue) and $Cu^{I}Zn$-MFU-4*l* (orange) at 298 K and a total pressure of 1 bar.

**Table 4. Summary of $H_2$ Adsorption Uptake, Isosteric Enthalpy of Adsorption for $H_2$, HD, and $D_2$, and Estimated Selectivity of Binary Mixtures of Hydrogen Isotope Molecules at Ambient Temperature for $Cu^{I}Zn$-MFU-4 and $Cu^{I}Zn$-MFU-4*l***

| | $H_2$ uptake at 1 bar and 298 K | | $-\Delta H_{ads}$ (kJ/mol)[a] ($-\Delta H°_{DFT}$)[b] | | | selectivity at 298 K[c] | | |
|---|---|---|---|---|---|---|---|---|
| | mmol/g | mol/L[d] | $H_2$ | HD | $D_2$ | $D_2/H_2$ | $HD/H_2$ | $D_2$/HD |
| $Cu^{I}Zn$-MFU-4 | 0.95 | 1.0 | 37.8 (29.3) | 39.0 (30.8) | 39.9 (31.8) | 1.35 | 1.20 | 1.12 |
| $Cu^{I}Zn$-MFU-4*l* | 1.0 | 0.51 | 33.1 (28.2) | 34.4 (30.0) | 35.7 (31.0) | 1.31 | 1.16 | 1.13 |

[a]Isosteric enthalpy of adsorption estimated by the Clausius–Clapeyron method for the $H_2$ loading of 0.50 mmol/g with adsorption data of 278–318 K. [b]Adsorption enthalpy calculated by DFT calculations for cluster models. [c]Calculated for an equimolar mixture (50/50) with the total pressure of 1 bar using the ideal adsorbed solution theory (IAST) with single-component adsorption isotherms collected for 278–318 K. [d]Calculated based on the crystallographic density of an activated framework.

The isosteric enthalpies of adsorption ($\Delta H_{ads}$) for HD and $D_2$ were calculated using the Clausius–Clapeyron method following the same procedure as discussed above for $H_2$. At a loading of 0.50 mmol/g in $Cu^{I}Zn$-MFU-4, the estimated $\Delta H_{ads}$ values for $D_2$ and HD were −39.9 and −39.0 kJ/mol, respectively, which are more exothermic compared with the value of −37.8 kJ/mol estimated for $H_2$ (Figure 8b and Table 4). The $Cu^{I}Zn$-MFU-4*l* framework showed $\Delta H_{ads}$ values of −35.7, −34.4, and −33.1 kJ/mol for $D_2$, HD, and $H_2$, respectively, under the same conditions. The slight increase in adsorption enthalpy for heavier isotopic gases aligns with expectations based on equilibrium

isotope effects[50] and also the trend reported in other porous adsorbents.[46,56] Indeed, DFT calculations for the cluster models indicate a similar magnitude of increase in adsorption enthalpies for heavier isotopic gases (Table 4).

We next evaluated gas selectivity using ideal adsorbed solution theory (IAST),[59] which is known to provide a reasonable estimate of the gas ratio in the adsorbed phase for a binary gas feed in porous materials, including metal–organic frameworks, across a wide range of gas mixtures.[98] Although IAST assumes common adsorption sites for the competing gases as well as site independence, these assumptions are likely valid for simulating hydrogen isotope separations. The gas molecules of interest ($H_2$, HD, and $D_2$) compete for the same adsorption sites through the same binding mechanism. Also, as observed in the $D_2$-dosed powder neutron diffraction study, $Cu^I\cdots Cu^I$ distances in $Cu^I$Zn-MFU-4 are not so close as to hinder adsorption at neighboring cluster sites. Selectivity ($S$) in a binary mixture of A and B is defined by $S = (x_A/x_B)/(y_A/y_B)$, where $x_A$ represents the fraction of component A in the adsorbed phase, $x_B$ ($= 1 - x_A$) represents the fraction of component B in the adsorbed phase, $y_A$ represents the fraction of component A in the gas phase, and $y_B$ ($= 1 - y_A$) represents the fraction of component B in the gas phase. Using IAST with the fit to the Langmuir–Freundlich model from the single-component isotherm data, we can estimate $x_A$ for a given gas feed ratio $y_A$ to obtain the selectivity $S$.

Estimated selectivities for 50/50 mixtures of $D_2/H_2$, $HD/H_2$, and $D_2$/HD at 1 bar and 298 K are, respectively, 1.35, 1.20, and 1.12 for $Cu^I$Zn-MFU-4, and 1.31, 1.16, and 1.13 for $Cu^I$Zn-MFU-4*l* (Table 4). Thus, $Cu^I$Zn-MFU-4 exhibits improved $D_2/H_2$ and $HD/H_2$ selectivity compared to $Cu^I$Zn-MFU-4*l*. The larger $D_2/H_2$ selectivity in $Cu^I$Zn-MFU-4 might be attributed to entropic factors (i.e., entropy of adsorption) because the difference in $\Delta H_{ads}$ between $D_2$ and $H_2$ is smaller for $Cu^I$Zn-MFU-4 than that of $Cu^I$Zn-MFU-4*l* (Table 4). The more favorable entropic factor for

$D_2/H_2$ selectivity in $Cu^{I}Zn$-MFU-4 could partly arise from the reduced π-backbonding interaction in $Cu^{I}Zn$-MFU-4 and therefore decreased metal–hydride bond character, which facilitate access to vibrational excitations for $D_2$ through low-energy librational and torsional modes. We note that the $D_2/H_2$ selectivity in $Cu^{I}Zn$-MFU-4 at 298 K is comparable to reported values obtained at much lower temperatures for existing adsorbents, such as $Ni_2$(dobdc) ($dobdc^{4-}$ = 2,5-dioxido-1,4-benzenedicarboxylate) for which $S$ = 1.4 at 150 K and 1 bar was estimated by IAST analysis (Figure 8c).[56]

**Investigations of Kinetic Isotope Effects on Adsorption and Desorption.** The selectivity estimated by IAST reflects a thermodynamic preference for adsorption of heavier isotopologues, associated with chemical affinity quantum sieving (CAQS).[49] Although the equilibrium isotope effects dominate ambient-temperature hydrogen isotope separations, we examined kinetic differences between $H_2$ and $D_2$ adsorption to assess whether kinetic effects could influence the separations under our experimental conditions. Both $Cu^{I}Zn$-MFU-4 and $Cu^{I}Zn$-MFU-4*l* reached $H_2$ adsorption equilibrium within ~20 s at 298 K under comparable sample masses (Figure 8d), suggesting that the smaller pore of $Cu^{I}Zn$-MFU-4 does not hinder the $H_2$ diffusion. Adsorption of $H_2$ and $D_2$ occurred at nearly the same rate at 298 K, but $D_2$ required a slightly longer time to reach the equilibrium capacity for both $Cu^{I}Zn$-MFU-4 and $Cu^{I}Zn$-MFU-4*l* (Figure S98). The adsorption kinetic isotope effects, estimated from the ratio of the effective adsorption rate constants for $H_2$ and $D_2$, were similar among $Cu^{I}Zn$-MFU-4, $Cu^{I}Zn$-MFU-4*l*, and ZnCl-MFU-4, which lacks open $Cu^{I}$ sites, and showed minimal temperature dependence over the ambient temperature range (278–318 K; Tables S28 and S29). Therefore, the slightly slower $D_2$ adsorption is likely to originate primarily from mass-transfer factors, including interparticle and intraparticle diffusion,[99] rather than from adsorption properties at the $Cu^{I}$ sites. However, since the estimated adsorption rate

depends on the amount of gas dosed and sample mass (see the SI for details), a rigorous comparison of the rate or kinetic isotope effects between $Cu^{I}$Zn-MFU-4 and $Cu^{I}$Zn-MFU-4*l* is beyond our scope.

Notably, the trend in the time required to reach adsorption equilibrium for $H_2$ versus $D_2$ is opposite to that reported under cryogenic temperatures (below 70 K) with porous adsorbents with small pores, where $H_2$ adsorption is kinetically impaired relative to that of $D_2$ due to kinetic quantum sieving (KQS) effects.[44,47,95] The inverted kinetic trend highlights a fundamental difference between the kinetic isotope effects for adsorption at ambient and cryogenic temperatures. Furthermore, the adsorption time scale in our materials at 298 K is on the order of several seconds, whereas porous materials that rely on KQS require several minutes due to slower diffusion associated with their small pores and low adsorption temperatures.[43,44] Therefore, ambient-temperature hydrogen isotope separations that do not rely on the KQS effect could inherently provide much faster adsorption kinetics at the material level, which in turn can enable higher gas throughput per unit time and a more efficient separation process.

We next analyzed the desorption kinetics of $H_2$ and $D_2$ at 298 K, which revealed slower $D_2$ desorption than $H_2$ for both $Cu^{I}$Zn-MFU-4 and $Cu^{I}$Zn-MFU-4*l* (Figure 8e). For example, the time required to obtain 90% desorption was ~80 and ~136 s for $H_2$ and $D_2$, respectively, for $Cu^{I}$Zn-MFU-4 at 298 K. The slower desorption of $D_2$ is rationalized by the classical mechanism of normal kinetic isotope effects with a weakly bonded transition state.[91,100] In particular, the lower zero-point energy of the $Cu^{I}$–$D_2$ vibrations relative to those of the $Cu^{I}$–$H_2$ species results in a thermodynamically more stable binding of $D_2$. Because the transition state of desorption has a weakened $Cu^{I}$–gas bond, it is less affected by differences in zero-point energy by isotope substitution, resulting in a larger activation barrier for $D_2$ dissociation due to its thermodynamically

more stable binding. This mechanism is analogous to chemical affinity quantum sieving (CAQS).[49] We anticipate that the desorption kinetic isotope effects become larger when adsorption is stronger, similarly to the equilibrium isotope effects by CAQS. The slower $D_2$ adsorption can help $D_2$ enrichment kinetically for pressure-swing processes by judiciously designing desorption conditions.

**Assessing Cascade Deuterium Enrichment Processes.** Although existing studies on hydrogen isotope separations mostly report their separation performance for the $D_2/H_2$ selectivity at a 50/50 ratio as a basic test, we note that an equal mixture of $D_2/H_2$ does not usually appear as a feed in industrial applications. Since the study of hydrogen isotope separations is driven by either deuterium production from natural abundance (0.015 mol D%) or recovery of nuclear fuel waste from deuterium–tritium reactors, we were motivated to analyze the properties of $Cu^{I}Zn$-MFU-4 for hydrogen isotope separations under conditions more relevant to these uses. Deuterium production was chosen for evaluation because the initial feed gas is simply a binary mixture of HD and $H_2$, which allows easier theoretical simulations via IAST than separations involving multi-component gas mixtures in nuclear fuel waste streams that may also contain tritium.

We assume that the initial feed for deuterium production from natural abundance is a 0.00030 /99.99970 ratio of $HD/H_2$, corresponding to 0.015 atom D%. Due to the extremely low concentration of HD, repeated cascade processes are required to gradually increase HD content, followed by isotopic equilibration with metal catalysts (such as palladium)[35,101] to convert HD into $H_2$ and $D_2$. We will focus on the initial HD enrichment steps to illustrate the cascade processes, since subsequent $D_2$ separations involve a ternary mixture of $D_2$, HD, and $H_2$, which complicates analysis and will be examined in future studies.

To examine selectivity during the repetitive HD enrichment cascade, we used IAST to analyze $HD/H_2$ selectivity values in $Cu^{I}Zn$-MFU-4 and $Cu^{I}Zn$-MFU-4*l* at different gas feed ratios, with a constant total pressure of 1 bar at 298 K. The $HD/H_2$ selectivities remained nearly constant, with a difference of less than ~0.01 from 0.00030/99.99970 to 99.9/0.1 (Figure S47), and therefore the selectivity estimated for a 50/50 mixture can represent the $HD/H_2$ selectivity for these compounds under these conditions. Next, we plotted the ratios of $HD/H_2$ in the adsorbed phase against the gas feed ratios to generate a McCabe–Thiele diagram,[57,58] which is traditionally used to estimate the theoretical number of equilibrium stages needed in binary distillations for target separations (Figure 8f). Note that, in the McCabe–Thiele diagram in Figure 8f, $x_A$ (the fraction of A in the adsorbed phase) is plotted on the *y*-axis, following the convention of the letters for the fraction in the adsorbed phase and gas phase. Typically, the enriched phase is plotted on the *y*-axis of the diagram.

When the $HD/H_2$ mixture with a 0.00030/99.99970 ratio is fed into the $Cu^{I}Zn$-MFU-4 framework, the $HD/H_2$ ratio in the adsorbed phase is expected to be 0.00036/99.99964. The adsorbed gas mixture will be desorbed and sent to the next stage as a feed gas to achieve a $HD/H_2$ ratio of 0.00043/99.99957 in the adsorbed phase. This process can be visualized in the McCabe–Thiele diagram by drawing a short horizontal line at the present $x_{HD}$ value (the HD fraction in the adsorbed phase on the *y*-axis) toward the diagonal line ($y = x$), transforming the current $x_{DH}$ value into the next $y_{HD}$ value (the ratio in the gas feed on the *x*-axis) and reflecting it onto the equilibrium curve with a short vertical line. This procedure visually provides the $x_{HD}$ value (on the *y*-axis) in the next stage. Repeating this calculation graphically enables estimation of the theoretical number of equilibrium stages needed to achieve the target $HD/H_2$ ratio. In this work, we estimated the theoretical number of equilibrium stages for four-fold enrichment from the natural abundance of

0.015 mol D% to 0.060 mol D% (i.e., from 0.030 HD% to 0.12 HD%), which is often used to characterize the efficiency of hydrogen enrichment processes.[34]

The McCabe–Thiele analysis demonstrates the theoretical stage numbers of 8 and 10 for $Cu^{I}$Zn-MFU-4 and $Cu^{I}$Zn-MFU-4*l*, respectively, for four-fold enrichment at 298 K and 1 bar. This result suggests that increasing the HD/$H_2$ selectivity from 1.16 in $Cu^{I}$Zn-MFU-4*l* to 1.20 in $Cu^{I}$Zn-MFU-4 could reduce the required number of stages in a cascade enrichment processes by about 20%. We do not compare these theoretical stage numbers with those of the existing technologies due to the simplicity of our analysis. Instead, we use the results specifically to compare the efficiency of deuterium enrichment between $Cu^{I}$Zn-MFU-4 and $Cu^{I}$Zn-MFU-4*l*. Furthermore, this analysis considers only the equilibrium selectivity to keep the discussion simple. The slower $D_2$ desorption could further increase the enrichment factor per step if desorption is performed after thermodynamic adsorption equilibration. However, we do not include kinetic contributions in our simulation because enrichment from kinetic isotope effects is highly sensitive to process design. For practical operations of deuterium extraction, the minimum requirement of the separation factor is proposed to be 1.1,[34] below which the required number of theoretical stages become impractically large. The separation factor is defined as the ratio of D/H in the enriched phase over D/H in the depleted phase, which must be distinguished from HD/$H_2$ selectivity. The HD/$H_2$ selectivity of 1.20 in $Cu^{I}$Zn-MFU-4 meets this criterion at low HD/$H_2$ ratios (specifically, below 60/40; see Table S10), supporting the feasibility of the initial deuterium enrichment from natural abundance after which an isotope equilibrator can split HD into $D_2$ and $H_2$ to perform subsequent $D_2$ purification.[102,103] Experiments intended to demonstrate room-temperature deuterium enrichment with $Cu^{I}$Zn-MFU-4 on a laboratory scale are currently underway via the design of a custom-build breakthrough apparatus and the scaling up of the material synthesis.

## Conclusions and Outlook

The foregoing results demonstrate the successful synthesis of $Cu^{I}$Zn-MFU-4, for which trigonal pyramidal $Cu^{I}$ sites are capable of engaging $H_2$ via orbital interactions upon adsorption. Detailed gas adsorption studies indicate that $H_2$ is adsorbed more strongly to $Cu^{I}$Zn-MFU-4 than its expanded version, $Cu^{I}$Zn-MFU-4*l* (−38 vs. −33 kJ/mol, respectively). While the increase in adsorption enthalpy from −33 to −38 kJ/mol is only about a 15% change, this degree of enhancement is still exceptional because $H_2$ adsorption enthalpies are generally unimpacted by minor linker modifications.[11,63,68,69] Spectroscopic and cluster-based computational studies revealed weaker π-backbonding but stronger σ-accepting interactions at the $Cu^{I}$ sites in $Cu^{I}$Zn-MFU-4 than those in $Cu^{I}$Zn-MFU-4*l* due to the more electron-deficient $bbta^{2-}$ linker compared to the $btdd^{2-}$ linker in the expanded material. However, the spectroscopic differences between these materials were much smaller than expected from the difference in hydrogen adsorption energy. Thus, a series of characterizations collectively corroborate pore confinement as the mechanism underlying the large enhancement of hydrogen adsorption in $Cu^{I}$Zn-MFU-4. Since our previous studies explored how geometric tuning of the metal substitution in the pentanuclear benzotriazolate cluster could modify $H_2$ binding properties,[14] this investigation of ultramicroporosity and linker effects provides further insights into controlling orbital-interaction-mediated $H_2$ adsorption at the trigonal pyramidal $Cu^{I}$ sites in the expanding family of MFU-4-type frameworks.[17,60,104–107]

Realization of the strongest $H_2$ adsorption enthalpy among porous adsorbents in $Cu^{I}$Zn-MFU-4, prompted us to consider the possibility of using it for hydrogen isotope enrichment at ambient temperatures through sequential cascades. This approach could separate hydrogen isotopes at lower energy costs than those required by existing adsorbents that only function at cryogenic

temperatures. Given that isotopic equilibration converting HD into $D_2$ and $H_2$ is proposed to occur at ambient temperature,[102,103] there are significant advantages to separating hydrogen isotopes under these conditions instead of cryogenic conditions. We developed an approach to estimate the performance of cascade enrichment processes under relevant conditions. Using the ideal adsorbed solution theory combined with a simple McCabe–Thiele analysis, we found that $Cu^{I}$Zn-MFU-4 could reduce the number of theoretical equilibrium stages by 20% for four-fold enrichment of HD from natural abundance, compared to $Cu^{I}$Zn-MFU-4*l*, despite only a slight increase in the HD/$H_2$ selectivity from 1.16 in $Cu^{I}$Zn-MFU-4*l* to 1.20 in $Cu^{I}$Zn-MFU-4. These analyses suggest that the number of theoretical stages is highly sensitive to selectivity, especially for values between 1 and 2. To realize efficient room temperature hydrogen isotope separations on an industrial scale, it will be necessary to define target values for selectivity and capacity under specific operating conditions, identify promising materials, and experimentally validate the predicted separation factors.

## ASSOCIATED CONTENT

The Supporting Information is available free of charge at http://pubs.acs.org.

Detailed experimental procedures, synthetic procedures, full characterizations of the reported compounds, full gas adsorption data, additional spectroscopic data, full neutron diffraction data, and computational information (PDF)

Adsorption information files (zip)

Cartesian coordinates of the optimized geometries of the computational cluster models (xyz)

Model structures of MFU-4 frameworks used for estimating pore volume (zip)

## Accession Codes

CCDC 2512672–2512677 contain the supplementary crystallographic data for this paper. These data can be obtained free of charge via www.ccdc.cam.ac.uk/data_request/cif, or by emailing data_request@ccdc.cam.ac.uk, or by contacting The Cambridge Crystallographic Data Centre, 12 Union Road, Cambridge CB2 1EZ, UK; fax: +44 1223 336033.

AUTHOR INFORMATION


### Corresponding Author

**Jeffrey R. Long** – *Department of Chemistry, Department of Chemical and Biomolecular Engineering, Department of Materials Science and Engineering, and Baker Hughes Institute for Decarbonization Materials, University of California, Berkeley, California 94720, United States; Materials Sciences Division, Lawrence Berkeley National Laboratory, Berkeley, California 94720, United States*; orcid.org/0000-0002-5324-1321; Email: jrlong@berkeley.edu

### Authors

**Yuto Yabuuchi** – *Department of Chemistry and Baker Hughes Institute for Decarbonization Materials, University of California, Berkeley, California 94720, United States; Materials Sciences Division, Lawrence Berkeley National Laboratory, Berkeley, California 94720, United States*; orcid.org/0000-0003-3034-558X

**Hiroyasu Furukawa** – *Department of Chemistry and Baker Hughes Institute for Decarbonization Materials, University of California, Berkeley, California 94720, United States; Materials Sciences Division, Lawrence Berkeley National Laboratory, Berkeley, California 94720, United States*; orcid.org/0000-0002-6082-1738

**Ryan A. Klein** – *Department of Chemistry and Baker Hughes Institute for Decarbonization Materials Material, University of California, Berkeley, California 94720, United States; Chemical, and Computational Sciences Directorate, National Renewable Energy Laboratory, Golden, Colorado 80401; Center for Neutron Research, National Institute of Standards and Technology, Gaithersburg, Maryland 20899, United States*; orcid.org/0000-0002-6807-6701

**Nikolay V. Tkachenko** – *Department of Chemistry and Baker Hughes Institute for Decarbonization Materials, University of California, Berkeley, California 94720, United States; Materials Sciences Division, Lawrence Berkeley National Laboratory, Berkeley, California 94720, United States; Department of Chemistry and Biochemistry, University of Oklahoma, Norman, Oklahoma, 73019, United States*; orcid.org/0000-0002-7296-4293

**N. Isaac Zakaria –** *Department of Chemical and Biomolecular Engineering and Baker Hughes Institute for Decarbonization Materials, University of California, Berkeley, California 94720, United States; Materials Sciences Division and Advanced Light Source, Lawrence Berkeley National Laboratory, Berkeley, California 94720, United States*; orcid.org/0000-0001-8990-1785

**Matthew N. Dods** – *Department of Chemical and Biomolecular Engineering and Baker Hughes Institute for Decarbonization Materials, University of California, Berkeley, California 94720, United States*

**Sarah L. Karstens** – *Department of Chemistry and Baker Hughes Institute for Decarbonization Materials, University of California, Berkeley, California 94720, United States; Materials Sciences Division, Lawrence Berkeley National Laboratory, Berkeley, California 94720, United States*; orcid.org/0000-0001-5847-0759

**Hyun June Moon** – *Center for Neutron Research, National Institute of Standards and Technology, Gaithersburg, Maryland 20899, United States; Department of Chemical and Biomolecular Engineering, University of Delaware, Newark, Delaware 19716, United States*

**My K. Vuong** – *Department of Chemistry and Baker Hughes Institute for Decarbonization Materials, University of California, Berkeley, California 94720, United States; Materials Sciences Division, Lawrence Berkeley National Laboratory, Berkeley, California 94720, United States*; orcid.org/0009-0002-0682-9728

**Matthew S. Santoso** – *Department of Chemical and Biomolecular Engineering and Baker Hughes Institute for Decarbonization Materials, University of California, Berkeley, California 94720, United States*; orcid.org/0000-0002-6002-9572

**Karina Riascos-Rodriguez** – *Chemical Sciences Division, Lawrence Berkeley National Laboratory, Berkeley, California 94720, United States*; orcid.org/0000-0001-6098-9744

**Kurtis M. Carsch** – *Department of Chemistry and Baker Hughes Institute for Decarbonization Materials, University of California, Berkeley, California 94720, United States*; orcid.org/0000-0003-4432-7518

**Hayden A. Evans** – *Center for Neutron Research, National Institute of Standards and Technology, Gaithersburg, Maryland 20899, United States*; orcid.org/0000-0002-1331-4274

**Yongqiang Cheng –** *Neutron Scattering Division, Oak Ridge National Laboratory, Oak Ridge, TN, United States*; orcid.org/0000-0002-3263-4812

**Denis Sheptyakov –** *Laboratory for Neutron Scattering and Imaging, Paul Scherrer Institut, CH-5232 Villigen PSI, Switzerland*

**Karen C. Bustillo** – *National Center for Electron Microscopy, Molecular Foundry, Lawrence Berkeley National Laboratory, Berkeley, CA, 94720, United States*; orcid.org/0000-0002-2096-6078

**Andrew M. Minor** – *Department of Materials Science and Engineering, University of California, Berkeley, California 94720, United States; National Center for Electron Microscopy, Molecular Foundry, Lawrence Berkeley National Laboratory, Berkeley, CA, 94720, United States*; orcid.org/0000-0003-3606-8309

**Walter S. Drisdell** – *Chemical Sciences Division, Lawrence Berkeley National Laboratory, Berkeley, California 94720, United States*; orcid.org/0000-0002-8693-4562

**Martin Head-Gordon** – *Department of Chemistry and Baker Hughes Institute for Decarbonization Materials, University of California, Berkeley, California 94720, United States; Chemical Sciences Division, Lawrence Berkeley National Laboratory, Berkeley, California 94720, United States*; orcid.org/0000-0002-4309-6669

**Craig M. Brown** – *Center for Neutron Research, National Institute of Standards and Technology, Gaithersburg, Maryland 20899, United States; Department of Chemical and Biomolecular Engineering, University of Delaware, Newark, Delaware 19716, United States*; orcid.org/0000-0002-9637-9355

**Notes**

The authors declare the following competing financial interest(s). Lawrence Berkeley National Laboratory has applied for a patent on some of the technology discussed here for hydrogen isotope separations, on which Y.Y. and J.R.L. are listed as co-inventors.

ACKNOWLEDGMENT

This research was supported by the Hydrogen Materials—Advanced Research Consortium (HyMARC), established as part of the Energy Materials Network under the U.S. Department of Energy (DOE), Hydrogen and Fuel Cell Technologies Office (HFTO), under Contract No. DE-AC02-05CH11231 with Lawrence Berkeley National Laboratory (LBNL). *In situ* gas-dosing Cu L-edge X-ray absorption spectroscopy data were collected at beamline 6.3.2 of the Advanced Light Source at LBNL, a user facility supported by the U.S. DOE, Office of Science under Contract No. DE-AC02-05CH11231. Electron microscopy was supported by the U.S. DOE, Office of Science, Basic Energy Sciences, Materials Sciences and Engineering Division under Contract No. DE-AC02-05CH11231 within the Electron Microscopy of Soft Matter Program (KC11BN) and carried out at the Molecular Foundry, which is supported by the U.S. DOE, Office of Science, Office of Basic Energy Sciences under Contract No. DE-AC02-05CH11231. Scanning electron microscopy by the Zeiss XB 550 was supported by NIH S10 Grant No. S10OD030258-01. Nuclear magnetic resonance instruments in this work were supported by the Pines Magnetic Resonance Center's Core NMR Facility. Powder neutron diffraction measurements were performed at the Swiss Spallation Neutron Source (SINQ), Paul Scherrer Institute, Villigen, Switzerland. Inelastic neutron scattering measurements were performed at the Spallation Neutron Source, a U.S. DOE, Office of Science User Facility operated by the Oak Ridge National Laboratory. Synchrotron powder X-ray diffraction data were collected at the 17-BM-B at the Advanced Photon Source, a U.S. DOE Office of Science user facility operated for the U.S. DOE Office of Science by Argonne National

Laboratory under Contract No. DE-AC02-06CH11357, and at BL02B2 in SPring-8 with the approval of the Japan Synchrotron Radiation Institute (JASRI) (Proposal No. 2024B2086). The Cu K-edge X-ray absorption spectroscopy experiments were performed at BL01B1 in SPring-8 with the approval of the JASRI (Proposal No. 2024A1765). We thank Dr. Henry Z. H. Jiang for helpful discussions with *in situ* gas-dosing infrared spectroscopy measurements, Dr. Tiffany Kinnibrugh for assistance with synchrotron powder X-ray diffraction measurements at the 17-BM-B, Dr. Yuki Mori for assistance with synchrotron powder X-ray diffraction measurements at BL02B2, Dr. Kazuo Kato and Dr. Misaki Katayama for assistance with Cu K-edge X-ray absorption spectroscopy at BL01B1, Mr. Juscelino B. Leão for assistance with powder neutron diffraction measurements, Dr. Misun Kang and the Electron Microscope Laboratory (EML) for assistance regarding scanning electron microscopy, Dr. Hasan Celik, Dr. Raynald Giovine, and the Core NMR Facility of the Pines Magnetic Resonance Center for assistance with NMR measurements, and Dr. Alexander J. Heyer and Adrian J. Huang for helpful discussions. N.V.T. acknowledges financial support from the University of Oklahoma startup fund and the OU Supercomputing Center for Education & Research (OSCER) for the computational resources. K.M.C. acknowledges financial support from the Arnold O. Beckman Foundation. R.A.K. acknowledges support from the U.S. DOE, HFTO under Contract No. DE-AC36-8GO28308 to the National Renewable Energy Laboratory, and support from the National Institute of Standards and Technology (NIST). M.K.V. and M.S.S. thank the support from the National Science Foundation Graduate Research Fellowship Program under Grant No. DGE 2146752. K.R.R. and W.S.D. acknowledge financial support from the U.S. DOE, Office of Science, Basic Energy Sciences, under FWP# CH19DRI01. H.J.M. acknowledges support from the cooperative agreement 70NANB20H133 from the NIST, U.S. Department of Commerce. H.A.E. and C.M.B.

were wholly supported by NIST. Any opinions, findings, and conclusions or recommendations expressed in this material are those of the author(s) and do not necessarily reflect the views of the National Science Foundation. Certain commercial equipment, instruments, or materials are identified in this document. Such identification does not imply recommendation or endorsement by the National Institute of Standards and Technology, nor does it imply that the products identified are necessarily the best available for the purpose.

REFERENCES

(1) Furukawa, H.; Cordova, K. E.; O'Keeffe, M.; Yaghi, O. M. The Chemistry and Applications of Metal–Organic Frameworks. *Science* **2013**, *341* (6149), 1230444. DOI: 10.1126/science.1230444.

(2) Chen, B.; Ockwig, N. W.; Millward, A. R.; Contreras, D. S.; Yaghi, O. M. High $H_2$ Adsorption in a Microporous Metal–Organic Framework with Open Metal Sites. *Angew. Chem. Int. Ed.* **2005**, *44* (30), 4745–4749. DOI: 10.1002/anie.200462787.

(3) Dincă, M.; Long, J. R. Hydrogen Storage in Microporous Metal–Organic Frameworks with Exposed Metal Sites. *Angew. Chem. Int. Ed.* **2008**, *47* (36), 6766–6779. DOI: 10.1002/anie.200801163.

(4) Suh, M. P.; Park, H. J.; Prasad, T. K.; Lim, D.-W. Hydrogen Storage in Metal–Organic Frameworks. *Chem. Rev.* **2012**, *112* (2), 782–835. DOI: 10.1021/cr200274s.

(5) Mason, J. A.; Veenstra, M.; Long, J. R. Evaluating Metal–Organic Frameworks for Natural Gas Storage. *Chem Sci* **2014**, *5* (1), 32–51. DOI: 10.1039/C3SC52633J.

(6) Yang, D.; Gates, B. C. Catalysis by Metal Organic Frameworks: Perspective and Suggestions for Future Research. *ACS Catal.* **2019**, *9* (3), 1779–1798. DOI: 10.1021/acscatal.8b04515.

(7) Iliescu, A.; Oppenheim, J. J.; Sun, C.; Dincă, M. Conceptual and Practical Aspects of Metal–Organic Frameworks for Solid–Gas Reactions. *Chem. Rev.* **2023**, *123* (9), 6197–6232. DOI: 10.1021/acs.chemrev.2c00537.

(8) Shustova, N. B.; Cozzolino, A. F.; Reineke, S.; Baldo, M.; Dincă, M. Selective Turn-On Ammonia Sensing Enabled by High-Temperature Fluorescence in Metal–Organic Frameworks with Open Metal Sites. *J. Am. Chem. Soc.* **2013**, *135* (36), 13326–13329. DOI: 10.1021/ja407778a.

(9) Chen, J.; Zhu, Y.; Kaskel, S. Porphyrin-Based Metal–Organic Frameworks for Biomedical Applications. *Angew. Chem. Int. Ed.* **2021**, *60* (10), 5010–5035. DOI: 10.1002/anie.201909880.

(10) Woellner, M.; Hausdorf, S.; Klein, N.; Mueller, P.; Smith, M. W.; Kaskel, S. Adsorption and Detection of Hazardous Trace Gases by Metal–Organic Frameworks. *Adv. Mater.* **2018**, *30* (37), 1704679. DOI: 10.1002/adma.201704679.

(11) Kapelewski, M. T.; Geier, S. J.; Hudson, M. R.; Stück, D.; Mason, J. A.; Nelson, J. N.; Xiao, D. J.; Hulvey, Z.; Gilmour, E.; FitzGerald, S. A.; Head-Gordon, M.; Brown, C. M.; Long, J. R. $M_2$(*m*-dobdc) (M = Mg, Mn, Fe, Co, Ni) Metal–Organic Frameworks Exhibiting Increased

Charge Density and Enhanced $H_2$ Binding at the Open Metal Sites. *J. Am. Chem. Soc.* **2014**, *136* (34), 12119–12129. DOI: 10.1021/ja506230r.

(12) Jaramillo, D. E.; Reed, D. A.; Jiang, H. Z. H.; Oktawiec, J.; Mara, M. W.; Forse, A. C.; Lussier, D. J.; Murphy, R. A.; Cunningham, M.; Colombo, V.; Shuh, D. K.; Reimer, J. A.; Long, J. R. Selective Nitrogen Adsorption via Backbonding in a Metal–Organic Framework with Exposed Vanadium Sites. *Nat. Mater.* **2020**, *19* (5), 517–521. DOI: 10.1038/s41563-019-0597-8.

(13) Jaramillo, D. E.; Jiang, H. Z. H.; Evans, H. A.; Chakraborty, R.; Furukawa, H.; Brown, C. M.; Head-Gordon, M.; Long, J. R. Ambient-Temperature Hydrogen Storage via Vanadium(II)–Dihydrogen Complexation in a Metal–Organic Framework. *J. Am. Chem. Soc.* **2021**, *143* (16), 6248–6256. DOI: 10.1021/jacs.1c01883.

(14) Yabuuchi, Y.; Furukawa, H.; Carsch, K. M.; Klein, R. A.; Tkachenko, N. V.; Huang, A. J.; Cheng, Y.; Taddei, K. M.; Novak, E.; Brown, C. M.; Head-Gordon, M.; Long, J. R. Geometric Tuning of Coordinatively Unsaturated Copper(I) Sites in Metal–Organic Frameworks for Ambient-Temperature Hydrogen Storage. *J. Am. Chem. Soc.* **2024**, *146* (32), 22759–22776. DOI: 10.1021/jacs.4c08039.

(15) Lee, K.; Isley, W. C.; Dzubak, A. L.; Verma, P.; Stoneburner, S. J.; Lin, L.-C.; Howe, J. D.; Bloch, E. D.; Reed, D. A.; Hudson, M. R.; Brown, C. M.; Long, J. R.; Neaton, J. B.; Smit, B.; Cramer, C. J.; Truhlar, D. G.; Gagliardi, L. Design of a Metal–Organic Framework with Enhanced Back Bonding for Separation of $N_2$ and $CH_4$. *J. Am. Chem. Soc.* **2014**, *136* (2), 698–704. DOI: 10.1021/ja4102979.

(16) Denysenko, D.; Grzywa, M.; Jelic, J.; Reuter, K.; Volkmer, D. Scorpionate-Type Coordination in MFU-4*l* Metal–Organic Frameworks: Small-Molecule Binding and Activation upon the Thermally Activated Formation of Open Metal Sites. *Angew. Chem. Int. Ed.* **2014**, *53* (23), 5832–5836. DOI: 10.1002/anie.201310004.

(17) Denysenko, D.; Grzywa, M.; Tonigold, M.; Streppel, B.; Krkljus, I.; Hirscher, M.; Mugnaioli, E.; Kolb, U.; Hanss, J.; Volkmer, D. Elucidating Gating Effects for Hydrogen Sorption in MFU-4-Type Triazolate-Based Metal–Organic Frameworks Featuring Different Pore Sizes. *Chem. Eur. J.* **2011**, *17* (6), 1837–1848. DOI: 10.1002/chem.201001872.

(18) Denysenko, D.; Werner, T.; Grzywa, M.; Puls, A.; Hagen, V.; Eickerling, G.; Jelic, J.; Reuter, K.; Volkmer, D. Reversible Gas-Phase Redox Processes Catalyzed by Co-Exchanged MFU-4*l*(arge). *Chem Commun* **2012**, *48* (9), 1236–1238. DOI: 10.1039/C2CC16235K.

(19) Denysenko, D.; Jelic, J.; Reuter, K.; Volkmer, D. Postsynthetic Metal and Ligand Exchange in MFU-4*l*: A Screening Approach toward Functional Metal–Organic Frameworks Comprising Single-Site Active Centers. *Chem. Eur. J.* **2015**, *21* (22), 8188–8199. DOI: 10.1002/chem.201406564.

(20) Wagen, C. Physics-Informed Machine Learning Enables Rapid Macroscopic pKa Prediction. Chemistry June 2, 2025. DOI: 10.26434/chemrxiv-2025-t8s9z-v2.

(21) Barnett, B. R.; Evans, H. A.; Su, G. M.; Jiang, H. Z. H.; Chakraborty, R.; Banyeretse, D.; Hartman, T. J.; Martinez, M. B.; Trump, B. A.; Tarver, J. D.; Dods, M. N.; Funke, L. M.; Börgel, J.; Reimer, J. A.; Drisdell, W. S.; Hurst, K. E.; Gennett, T.; FitzGerald, S. A.; Brown, C. M.; Head-Gordon, M.; Long, J. R. Observation of an Intermediate to $H_2$ Binding in a Metal–Organic Framework. *J. Am. Chem. Soc.* **2021**, *143* (36), 14884–14894. DOI: 10.1021/jacs.1c07223.

(22) Mohamed, M. H.; Yang, Y.; Li, L.; Zhang, S.; Ruffley, J. P.; Jarvi, A. G.; Saxena, S.; Veser, G.; Johnson, J. K.; Rosi, N. L. Designing Open Metal Sites in Metal–Organic Frameworks

for Paraffin/Olefin Separations. *J. Am. Chem. Soc.* **2019**, *141* (33), 13003–13007. DOI: 10.1021/jacs.9b06582.
(23) Carsch, K. M.; Huang, A. J.; Dods, M. N.; Parker, S. T.; Rohde, R. C.; Jiang, H. Z. H.; Yabuuchi, Y.; Karstens, S. L.; Kwon, H.; Chakraborty, R.; Bustillo, K. C.; Meihaus, K. R.; Furukawa, H.; Minor, A. M.; Head-Gordon, M.; Long, J. R. Selective Adsorption of Oxygen from Humid Air in a Metal–Organic Framework with Trigonal Pyramidal Copper(I) Sites. *J. Am. Chem. Soc.* **2024**, *146* (5), 3160–3170. DOI: 10.1021/jacs.3c10753.
(24) Zhang, F.; Zhao, Z.; Wang, Y.; Li, X.; Bai, X.; Lu, M.; Wang, Y.; Wang, X.; Li, L.; Li, J.; Yang, J. Nitrogen Adsorption Sites with Low Polarizability for Benchmark $N_2/CH_4$ Separation. *Angew. Chem. Int. Ed.* **2025**, *64* (36), e202510242. DOI: 10.1002/anie.202510242.
(25) Tkachenko, N. V.; Yabuuchi, Y.; Carsch, K. M.; Furukawa, H.; Long, J. R.; Head-Gordon, M. Computational Optimization of Room Temperature Usable Capacity for Hydrogen Storage in MFU-4-Type Metal–Organic Frameworks via Pairwise Metal Substitutions. *J. Phys. Chem. C* **2025**, *129* (1), 167–178. DOI: 10.1021/acs.jpcc.4c07631.
(26) Adil, K.; Belmabkhout, Y.; Pillai, R. S.; Cadiau, A.; Bhatt, P. M.; Assen, A. H.; Maurin, G.; Eddaoudi, M. Gas/Vapour Separation Using Ultra-Microporous Metal–Organic Frameworks: Insights into the Structure/Separation Relationship. *Chem. Soc. Rev.* **2017**, *46* (11), 3402–3430. DOI: 10.1039/C7CS00153C.
(27) Wang, T.; Lin, E.; Peng, Y.-L.; Chen, Y.; Cheng, P.; Zhang, Z. Rational Design and Synthesis of Ultramicroporous Metal–Organic Frameworks for Gas Separation. *Coord. Chem. Rev.* **2020**, *423*, 213485. DOI: 10.1016/j.ccr.2020.213485.
(28) Mukherjee, S.; Sikdar, N.; O'Nolan, D.; Franz, D. M.; Gascón, V.; Kumar, A.; Kumar, N.; Scott, H. S.; Madden, D. G.; Kruger, P. E.; Space, B.; Zaworotko, M. J. Trace $CO_2$ Capture by an Ultramicroporous Physisorbent with Low Water Affinity. *Sci. Adv.* **2019**, *5* (11), eaax9171. DOI: 10.1126/sciadv.aax9171.
(29) Kitagawa, S.; Matsuda, R. Chemistry of Coordination Space of Porous Coordination Polymers. *Coord. Chem. Rev.* **2007**, *251* (21–24), 2490–2509. DOI: 10.1016/j.ccr.2007.07.009.
(30) Kitaura, R.; Kitagawa, S.; Kubota, Y.; Kobayashi, T. C.; Kindo, K.; Mita, Y.; Matsuo, A.; Kobayashi, M.; Chang, H.-C.; Ozawa, T. C.; Suzuki, M.; Sakata, M.; Takata, M. Formation of a One-Dimensional Array of Oxygen in a Microporous Metal–Organic Solid. *Science* **2002**, *298* (5602), 2358–2361. DOI: 10.1126/science.1078481.
(31) Matsuda, R.; Kitaura, R.; Kitagawa, S.; Kubota, Y.; Belosludov, R. V.; Kobayashi, T. C.; Sakamoto, H.; Chiba, T.; Takata, M.; Kawazoe, Y.; Mita, Y. Highly Controlled Acetylene Accommodation in a Metal–Organic Microporous Material. *Nature* **2005**, *436* (7048), 238–241. DOI: 10.1038/nature03852.
(32) Everett, D. H.; Powl, J. C. Adsorption in Slit-like and Cylindrical Micropores in the Henry's Law Region. A Model for the Microporosity of Carbons. *J. Chem. Soc. Faraday Trans. 1 Phys. Chem. Condens. Phases* **1976**, *72* (0), 619. DOI: 10.1039/f19767200619.
(33) Pan, L.; Sander, M. B.; Huang, X.; Li, J.; Smith, M.; Bittner, E.; Bockrath, B.; Johnson, J. K. Microporous Metal Organic Materials: Promising Candidates as Sorbents for Hydrogen Storage. *J. Am. Chem. Soc.* **2004**, *126* (5), 1308–1309. DOI: 10.1021/ja0392871.
(34) *Separation of Hydrogen Isotopes*; Rae, H. K., Ed.; ACS Symposium Series; American Chemical Society: Washington, D. C., 1978; Vol. 68. DOI: 10.1021/bk-1978-0068.

(35) Perevezentsev, A.; Rozenkevich, M. *Tritium Technologies for Thermonuclear Fusion Reactors*; Elsevier, 2021. DOI: 10.1016/C2020-0-01246-6.
(36) Lyding, J. W.; Hess, K.; Kizilyalli, I. C. Reduction of Hot Electron Degradation in Metal Oxide Semiconductor Transistors by Deuterium Processing. *Appl. Phys. Lett.* **1996**, *68* (18), 2526–2528. DOI: 10.1063/1.116172.
(37) Haggin, J. Deuterium Processing Stabilizes Silicon Semiconductor Devices. *Chem. Eng. News Arch.* **1996**, *74* (12), 25. DOI: 10.1021/cen-v074n012.p025.
(38) Pirali, T.; Serafini, M.; Cargnin, S.; Genazzani, A. A. Applications of Deuterium in Medicinal Chemistry. *J. Med. Chem.* **2019**, *62* (11), 5276–5297. DOI: 10.1021/acs.jmedchem.8b01808.
(39) Team, J. Fusion Energy Production from a Deuterium–Tritium Plasma in the JET Tokamak. *Nucl. Fusion* **1992**, *32* (2), 187–203. DOI: 10.1088/0029-5515/32/2/I01.
(40) Glugla, M.; Antipenkov, A.; Beloglazov, S.; Caldwell-Nichols, C.; Cristescu, I. R.; Cristescu, I.; Day, C.; Doerr, L.; Girard, J.-P.; Tada, E. The ITER Tritium Systems. *Fusion Eng. Des.* **2007**, *82* (5–14), 472–487. DOI: 10.1016/j.fusengdes.2007.02.025.
(41) Beenakker, J. J. M.; Borman, V. D.; Krylov, S. Yu. Molecular Transport in Subnanometer Pores: Zero-Point Energy, Reduced Dimensionality and Quantum Sieving. *Chem. Phys. Lett.* **1995**, *232* (4), 379–382. DOI: 10.1016/0009-2614(94)01372-3.
(42) Chen, B.; Zhao, X.; Putkham, A.; Hong, K.; Lobkovsky, E. B.; Hurtado, E. J.; Fletcher, A. J.; Thomas, K. M. Surface Interactions and Quantum Kinetic Molecular Sieving for $H_2$ and $D_2$ Adsorption on a Mixed Metal−Organic Framework Material. *J. Am. Chem. Soc.* **2008**, *130* (20), 6411–6423. DOI: 10.1021/ja710144k.
(43) Teufel, J.; Oh, H.; Hirscher, M.; Wahiduzzaman, M.; Zhechkov, L.; Kuc, A.; Heine, T.; Denysenko, D.; Volkmer, D. MFU-4 – A Metal–Organic Framework for Highly Effective $H_2/D_2$ Separation. *Adv. Mater.* **2013**, *25* (4), 635–639. DOI: 10.1002/adma.201203383.
(44) Liu, M.; Zhang, L.; Little, M. A.; Kapil, V.; Ceriotti, M.; Yang, S.; Ding, L.; Holden, D. L.; Balderas-Xicohténcatl, R.; He, D.; Clowes, R.; Chong, S. Y.; Schütz, G.; Chen, L.; Hirscher, M.; Cooper, A. I. Barely Porous Organic Cages for Hydrogen Isotope Separation. *Science* **2019**, *366* (6465), 613–620. DOI: 10.1126/science.aax7427.
(45) FitzGerald, S. A.; Burkholder, B.; Friedman, M.; Hopkins, J. B.; Pierce, C. J.; Schloss, J. M.; Thompson, B.; Rowsell, J. L. C. Metal-Specific Interactions of $H_2$ Adsorbed within Isostructural Metal–Organic Frameworks. *J. Am. Chem. Soc.* **2011**, *133* (50), 20310–20318. DOI: 10.1021/ja2071384.
(46) Weinrauch, I.; Savchenko, I.; Denysenko, D.; Souliou, S. M.; Kim, H.-H.; Le Tacon, M.; Daemen, L. L.; Cheng, Y.; Mavrandonakis, A.; Ramirez-Cuesta, A. J.; Volkmer, D.; Schütz, G.; Hirscher, M.; Heine, T. Capture of Heavy Hydrogen Isotopes in a Metal–Organic Framework with Active Cu(I) Sites. *Nat. Commun.* **2017**, *8* (1), 14496. DOI: 10.1038/ncomms14496.
(47) FitzGerald, S. A.; Mukasa, D.; Rigdon, K. H.; Zhang, N.; Barnett, B. R. Hydrogen Isotope Separation within the Metal–Organic Framework Cu(I)-MFU-4*l*. *J. Phys. Chem. C* **2019**, *123* (50), 30427–30433. DOI: 10.1021/acs.jpcc.9b09332.
(48) Kapelewski, M. T.; Runčevski, T.; Tarver, J. D.; Jiang, H. Z. H.; Hurst, K. E.; Parilla, P. A.; Ayala, A.; Gennett, T.; FitzGerald, S. A.; Brown, C. M.; Long, J. R. Record High Hydrogen Storage Capacity in the Metal–Organic Framework $Ni_2$(*m*-dobdc) at Near-Ambient Temperatures. *Chem. Mater.* **2018**, *30* (22), 8179–8189. DOI: 10.1021/acs.chemmater.8b03276.

(49) Savchenko, I.; Mavrandonakis, A.; Heine, T.; Oh, H.; Teufel, J.; Hirscher, M. Hydrogen Isotope Separation in Metal–Organic Frameworks: Kinetic or Chemical Affinity Quantum-Sieving? *Microporous Mesoporous Mater.* **2015**, *216*, 133–137. DOI: 10.1016/j.micromeso.2015.03.017.
(50) Bender, B. R.; Kubas, G. J.; Jones, L. H.; Swanson, B. I.; Eckert, J.; Capps, K. B.; Hoff, C. D. Why Does $D_2$ Bind Better Than $H_2$? A Theoretical and Experimental Study of the Equilibrium Isotope Effect on $H_2$ Binding in a M($\eta^2$-$H_2$) Complex. Normal Coordinate Analysis of $W(CO)_3(PCy_3)_2(\eta^2\text{-}H_2)$. *J. Am. Chem. Soc.* **1997**, *119* (39), 9179–9190. DOI: 10.1021/ja971009c.
(51) Parkin, G. Temperature-Dependent Transitions Between Normal and Inverse Isotope Effects Pertaining to the Interaction of H−H and C−H Bonds with Transition Metal Centers. *Acc. Chem. Res.* **2009**, *42* (2), 315–325. DOI: 10.1021/ar800156h.
(52) Abu-Hasanayn, F.; Krogh-Jespersen, K.; Goldman, A. S. Theoretical Study of Primary and Secondary Deuterium Equilibrium Isotope Effects for Hydrogen and Methane Addition to Iridium Complex *trans*-$Ir(PR_3)_2(CO)X$. *J. Am. Chem. Soc.* **1993**, *115* (18), 8019–8023. DOI: 10.1021/ja00071a012.
(53) Janak, K. E.; Parkin, G. Deuterium and Tritium Equilibrium Isotope Effects for Coordination and Oxidative Addition of Dihydrogen to $[W(CO)_5]$ and for the Interconversion of $W(CO)_5(\eta^2\text{-}H_2)$ and $W(CO)_5H_2$. *Organometallics* **2003**, *22* (22), 4378–4380. DOI: 10.1021/om0303810.
(54) Kitayama, T.; Yamauchi, T.; Uchida, K.; Tanaka, S.; Toyoda, R.; Iguchi, H.; Sakamoto, R.; Xue, H.; Kishimoto, N.; Yoshida, T.; Uruga, T.; Noro, S.; Takaishi, S. Hydrogen Isotope Separation at Exceptionally High Temperature Using an Unsaturated Organometallic Complex. *Dalton Trans.* **2025**, *54* (6), 2621–2627. DOI: 10.1039/D4DT03018D.
(55) Yamauchi, T.; Kitayama, T.; Uchida, K.; Keuzenkamp, N.; Iguchi, H.; Toyoda, R.; Sakamoto, R.; Xue, H.; Kishimoto, N.; Noro, S.; Takaishi, S. Room-Temperature Chromatographic $H_2/D_2$ Separation *via* a Solid Dihydrogen Complex with Balanced Thermodynamics and Kinetics. *Green Chem.* **2026**, *28*, 1507–1513. DOI: 10.1039/D5GC04476F.
(56) FitzGerald, S. A.; Pierce, C. J.; Rowsell, J. L. C.; Bloch, E. D.; Mason, J. A. Highly Selective Quantum Sieving of $D_2$ from $H_2$ by a Metal–Organic Framework As Determined by Gas Manometry and Infrared Spectroscopy. *J. Am. Chem. Soc.* **2013**, *135* (25), 9458–9464. DOI: 10.1021/ja402103u.
(57) Mccabe, W. L.; Thiele, E. W. Graphical Design of Fractionating Columns. *Ind. Eng. Chem.* **1925**, *17* (6), 605–611. DOI: 10.1021/ie50186a023.
(58) Jirasek, F.; Lenhard, J.; Heiß, J.; Hasse, H. The McCabe–Thiele Method: A Centenary Tribute to an Emblem of Chemical Engineering and Engineering Epistemology. *Ind. Eng. Chem. Res.* **2025**, *64* (39), 18979–18988. DOI: 10.1021/acs.iecr.5c02730.
(59) Myers, A. L.; Prausnitz, J. M. Thermodynamics of Mixed-Gas Adsorption. *AIChE J.* **1965**, *11* (1), 121–127. DOI: 10.1002/aic.690110125.
(60) Biswas, S.; Grzywa, M.; Nayek, H. P.; Dehnen, S.; Senkovska, I.; Kaskel, S.; Volkmer, D. A Cubic Coordination Framework Constructed from Benzobistriazolate Ligands and Zinc Ions Having Selective Gas Sorption Properties. *Dalton Trans.* **2009**, No. 33, 6487. DOI: 10.1039/b904280f.
(61) Sengupta, D.; Melix, P.; Bose, S.; Duncan, J.; Wang, X.; Mian, M. R.; Kirlikovali, K. O.; Joodaki, F.; Islamoglu, T.; Yildirim, T.; Snurr, R. Q.; Farha, O. K. Air-Stable Cu(I) Metal–

Organic Framework for Hydrogen Storage. *J. Am. Chem. Soc.* **2023**, *145* (37), 20492–20502. DOI: 10.1021/jacs.3c06393.
(62) Cai, Z.; Bien, C. E.; Liu, Q.; Wade, C. R. Insights into $CO_2$ Adsorption in M–OH Functionalized MOFs. *Chem. Mater.* **2020**, *32* (10), 4257–4264. DOI: 10.1021/acs.chemmater.0c00746.
(63) Oppenheim, J. J.; Mancuso, J. L.; Wright, A. M.; Rieth, A. J.; Hendon, C. H.; Dincă, M. Divergent Adsorption Behavior Controlled by Primary Coordination Sphere Anions in the Metal–Organic Framework $Ni_2X_2$BTDD. *J. Am. Chem. Soc.* **2021**, *143* (40), 16343–16347. DOI: 10.1021/jacs.1c07449.
(64) Brozek, C. K.; Dincă, M. Thermodynamic Parameters of Cation Exchange in MOF-5 and MFU-4*l*. *Chem. Commun.* **2015**, *51* (59), 11780–11782. DOI: 10.1039/C5CC04249F.
(65) Breck, D. W. *Zeolite Molecular Sieves: Structure, Chemistry, and Use*; A Wiley-interscience publication; Wiley: New York, NY, 1974.
(66) Mehio, N.; Dai, S.; Jiang, D. Quantum Mechanical Basis for Kinetic Diameters of Small Gaseous Molecules. *J. Phys. Chem. A* **2014**, *118* (6), 1150–1154. DOI: 10.1021/jp412588f.
(67) Baker, M. L.; Mara, M. W.; Yan, J. J.; Hodgson, K. O.; Hedman, B.; Solomon, E. I. K- and L-Edge X-Ray Absorption Spectroscopy (XAS) and Resonant Inelastic X-Ray Scattering (RIXS) Determination of Differential Orbital Covalency (DOC) of Transition Metal Sites. *Coord. Chem. Rev.* **2017**, *345*, 182–208. DOI: 10.1016/j.ccr.2017.02.004.
(68) Gygi, D.; Bloch, E. D.; Mason, J. A.; Hudson, M. R.; Gonzalez, M. I.; Siegelman, R. L.; Darwish, T. A.; Queen, W. L.; Brown, C. M.; Long, J. R. Hydrogen Storage in the Expanded Pore Metal–Organic Frameworks $M_2$(dobpdc) (M = Mg, Mn, Fe, Co, Ni, Zn). *Chem. Mater.* **2016**, *28* (4), 1128–1138. DOI: 10.1021/acs.chemmater.5b04538.
(69) Sumida, K.; Stück, D.; Mino, L.; Chai, J.-D.; Bloch, E. D.; Zavorotynska, O.; Murray, L. J.; Dincă, M.; Chavan, S.; Bordiga, S.; Head-Gordon, M.; Long, J. R. Impact of Metal and Anion Substitutions on the Hydrogen Storage Properties of M-BTT Metal–Organic Frameworks. *J. Am. Chem. Soc.* **2013**, *135* (3), 1083–1091. DOI: 10.1021/ja310173e.
(70) Fischer, P.; Frey, G.; Koch, M.; Könnecke, M.; Pomjakushin, V.; Schefer, J.; Thut, R.; Schlumpf, N.; Bürge, R.; Greuter, U.; Bondt, S.; Berruyer, E. High-Resolution Powder Diffractometer HRPT for Thermal Neutrons at SINQ. *Phys. B Condens. Matter* **2000**, *276–278*, 146–147. DOI: 10.1016/S0921-4526(99)01399-X.
(71) Wu, H.; Zhou, W.; Yildirim, T. Hydrogen Storage in a Prototypical Zeolitic Imidazolate Framework-8. *J. Am. Chem. Soc.* **2007**, *129* (17), 5314–5315. DOI: 10.1021/ja0691932.
(72) Klein, R. A.; Evans, H. A.; Trump, B. A.; Udovic, T. J.; Brown, C. M. Neutron Scattering Studies of Materials for Hydrogen Storage. In *Comprehensive Inorganic Chemistry III*; Elsevier, 2023; pp 3–50. DOI: 10.1016/B978-0-12-823144-9.00028-5.
(73) Hyeon-Deuk, K.; Ando, K. Correlations of Intra- and Intermolecular Dynamics and Structure in Liquid Para-Hydrogen. *Phys. Rev. B* **2014**, *90* (16), 165132. DOI: 10.1103/PhysRevB.90.165132.
(74) Stoicheff, B. P. High Resolution Raman Spectroscopy of Gases: IX. Spectra of $H_2$, HD, and $D_2$. *Can. J. Phys.* **1957**, *35* (6), 730–741. DOI: 10.1139/p57-079.
(75) George, M. W.; Haward, M. T.; Hamley, P. A.; Hughes, C.; Johnson, F. P. A.; Popov, V. K.; Poliakoff, M. Infrared Spectroscopic Study of the Photochemical Substitution and Oxidative Addition Reactions of ($\eta^5$-$C_5R_5$)M(CO)$_4$ Compounds of Group 5 Metals: Characterization of the Products of Reaction with Nitrogen, Hydrogen and $HSiEt_{3-x}Cl_x$ and the Kinetic

Investigation of ($\eta^5$-$C_5R_5$)M(CO)$_3$ Intermediates. *J. Am. Chem. Soc.* **1993**, *115* (6), 2286–2299. DOI: 10.1021/ja00059a026.
(76) Eckert, J.; Kubas, G. J. Barrier to Rotation of the Dihydrogen Ligand in Metal Complexes. *J. Phys. Chem.* **1993**, *97* (10), 2378–2384. DOI: 10.1021/j100112a044.
(77) Su, G. M.; Wang, H.; Barnett, B. R.; Long, J. R.; Prendergast, D.; Drisdell, W. S. Backbonding Contributions to Small Molecule Chemisorption in a Metal–Organic Framework with Open Copper(I) Centers. *Chem. Sci.* **2021**, *12* (6), 2156–2164. DOI: 10.1039/D0SC06038K.
(78) Wang, H.; Su, G. M.; Barnett, B. R.; Drisdell, W. S.; Long, J. R.; Prendergast, D. Understanding 2p Core-Level Excitons of Late Transition Metals by Analysis of Mixed-Valence Copper in a Metal–Organic Framework. *Phys. Chem. Chem. Phys.* **2024**, *26* (15), 11980–11987. DOI: 10.1039/D4CP00662C.
(79) Harkins, S. B.; Mankad, N. P.; Miller, A. J. M.; Szilagyi, R. K.; Peters, J. C. Probing the Electronic Structures of $[Cu_2(\mu\text{-}XR_2)]^{n+}$ Diamond Cores as a Function of the Bridging X Atom (X = N or P) and Charge ($n$ = 0, 1, 2). *J. Am. Chem. Soc.* **2008**, *130* (11), 3478–3485. DOI: 10.1021/ja076537v.
(80) George, S. J.; Lowery, M. D.; Solomon, E. I.; Cramer, S. P. Copper L-Edge Spectral Studies: A Direct Experimental Probe of the Ground-State Covalency in the Blue Copper Site in Plastocyanin. *J. Am. Chem. Soc.* **1993**, *115* (7), 2968–2969. DOI: 10.1021/ja00060a052.
(81) Hocking, R. K.; George, S. D.; Gross, Z.; Walker, F. A.; Hodgson, K. O.; Hedman, B.; Solomon, E. I. Fe L- and K-Edge XAS of Low-Spin Ferric Corrole: Bonding and Reactivity Relative to Low-Spin Ferric Porphyrin. *Inorg. Chem.* **2009**, *48* (4), 1678–1688. DOI: 10.1021/ic802248t.
(82) Najibi, A.; Goerigk, L. DFT-D4 Counterparts of Leading META-Generalized-gradient Approximation and Hybrid Density Functionals for Energetics and Geometries. *J. Comput. Chem.* **2020**, *41* (30), 2562–2572. DOI: 10.1002/jcc.26411.
(83) Weigend, F.; Ahlrichs, R. Balanced Basis Sets of Split Valence, Triple Zeta Valence and Quadruple Zeta Valence Quality for H to Rn: Design and Assessment of Accuracy. *Phys. Chem. Chem. Phys.* **2005**, *7* (18), 3297. DOI: 10.1039/b508541a.
(84) Horn, P. R.; Mao, Y.; Head-Gordon, M. Probing Non-Covalent Interactions with a Second Generation Energy Decomposition Analysis Using Absolutely Localized Molecular Orbitals. *Phys. Chem. Chem. Phys.* **2016**, *18* (33), 23067–23079. DOI: 10.1039/C6CP03784D.
(85) Levine, D. S.; Head-Gordon, M. Energy Decomposition Analysis of Single Bonds within Kohn–Sham Density Functional Theory. *Proc. Natl. Acad. Sci.* **2017**, *114* (48), 12649–12656. DOI: 10.1073/pnas.1715763114.
(86) Mao, Y.; Loipersberger, M.; Horn, P. R.; Das, A.; Demerdash, O.; Levine, D. S.; Prasad Veccham, S.; Head-Gordon, T.; Head-Gordon, M. From Intermolecular Interaction Energies and Observable Shifts to Component Contributions and Back Again: A Tale of Variational Energy Decomposition Analysis. *Annu. Rev. Phys. Chem.* **2021**, *72* (1), 641–666. DOI: 10.1146/annurev-physchem-090419-115149.
(87) Kubas, G. J. Fundamentals of $H_2$ Binding and Reactivity on Transition Metals Underlying Hydrogenase Function and $H_2$ Production and Storage. *Chem. Rev.* **2007**, *107* (10), 4152–4205. DOI: 10.1021/cr050197j.
(88) Turner, J. J.; Poliakoff, M.; Howdle, S. M.; Jackson, S. A.; McLaughlin, J. G. Infrared Spectroscopy and Chemistry in Liquid Rare-Gas Solvents. *Faraday Discuss. Chem. Soc.* **1988**, *86*, 271. DOI: 10.1039/dc9888600271.

(89) Cavenati, S.; Grande, C. A.; Rodrigues, A. E. Removal of Carbon Dioxide from Natural Gas by Vacuum Pressure Swing Adsorption. *Energy Fuels* **2006**, *20* (6), 2648–2659. DOI: 10.1021/ef060119e.
(90) Ko, D.; Siriwardane, R.; Biegler, L. T. Optimization of Pressure Swing Adsorption and Fractionated Vacuum Pressure Swing Adsorption Processes for $CO_2$ Capture. *Ind. Eng. Chem. Res.* **2005**, *44* (21), 8084–8094. DOI: 10.1021/ie050012z.
(91) *Isotope Effects in Chemical Reactions*; Collins, C. J., Bowman, N. S., Eds.; Van Nostrand Reinhold Company: New York, 1971.
(92) McLennan, D. J. Model Calculations of Secondary Isotope Effects. In *Secondary and solvent isotope effects*; Isotopes in organic chemistry; E. Buncel Ed.; Elsevier: Amsterdam, 1987; pp 393–480.
(93) Stéphanie-Victoire, F.; Goulay, A.-M.; Cohen De Lara, E. Adsorption and Coadsorption of Molecular Hydrogen Isotopes in Zeolites. 1. Isotherms of $H_2$, HD, and $D_2$ in NaA by Thermomicrogravimetry. *Langmuir* **1998**, *14* (25), 7255–7259. DOI: 10.1021/la980521o.
(94) Zhang, L.; Röß-Ohlenroth, R.; Peterson, V. K.; Duyker, S. G.; Li, C.; Fiorio, J. L.; Joswig, J.-O.; Dinnebier, R.; Volkmer, D.; Hirscher, M. Isotopologue-Induced Structural Dynamics of a Triazolate Metal–Organic Framework for Efficient Hydrogen Isotope Separation. *Nat. Commun.* **2025**, *16* (1), 5941. DOI: 10.1038/s41467-025-61107-3.
(95) Kim, J. Y.; Zhang, L.; Balderas-Xicohténcatl, R.; Park, J.; Hirscher, M.; Moon, H. R.; Oh, H. Selective Hydrogen Isotope Separation via Breathing Transition in MIL-53(Al). *J. Am. Chem. Soc.* **2017**, *139* (49), 17743–17746. DOI: 10.1021/jacs.7b10323.
(96) Jung, M.; Park, J.; Muhammad, R.; Park, T.; Jung, S.-Y.; Yi, J.; Jung, C.; Ollivier, J.; Ramirez-Cuesta, A. J.; Park, J. T.; Kim, J.; Russina, M.; Oh, H. Lattice-Driven Gating in a Cu-Based Zeolitic Imidazolate Framework for Efficient High-Temperature Hydrogen Isotope Separation. *Nat. Commun.* **2025**, *16* (1), 2032. DOI: 10.1038/s41467-025-56649-5.
(97) Sugiyama, T.; Asakura, Y.; Uda, T.; Kotoh, K. Measurement of Breakthrough Curves on Pressure Swing Adsorption for Hydrogen Isotope Separation. *Fusion Sci. Technol.* **2005**, *48* (1), 163–166. DOI: 10.13182/fst05-a904.
(98) Krishna, R.; Van Baten, J. M. In Silico Screening of Metal–Organic Frameworks in Separation Applications. *Phys. Chem. Chem. Phys.* **2011**, *13* (22), 10593. DOI: 10.1039/c1cp20282k.
(99) Kast, W.; Hohenthanner, C.-R. Mass Transfer within the Gas-Phase of Porous Media. *Int. J. Heat Mass Transf.* **2000**, *43* (5), 807–823. DOI: 10.1016/S0017-9310(99)00158-1.
(100) Wiberg, K. B. The Deuterium Isotope Effect. *Chem. Rev.* **1955**, *55* (4), 713–743. DOI: 10.1021/cr50004a004.
(101) Souers, P. C. *Hydrogen Properties for Fusion Energy*; University of California Press, 1986. DOI: 10.1525/9780520338401.
(102) Noh, J.; Fulgueras, A. M.; Sebastian, L. J.; Lee, H. G.; Kim, D. S.; Cho, J. Estimation of Thermodynamic Properties of Hydrogen Isotopes and Modeling of Hydrogen Isotope Systems Using Aspen Plus Simulator. *J. Ind. Eng. Chem.* **2017**, *46*, 1–8. DOI: 10.1016/j.jiec.2016.07.053.
(103) Perevezentsev, A.; Rozenkevich, M. Thermodynamic and Kinetic Characteristics of Isotope Separation Processes. In *Tritium Technologies for Thermonuclear Fusion Reactors*; Elsevier, 2021; pp 99–132. DOI: 10.1016/B978-0-12-824322-0.00004-8.
(104) Schmieder, P.; Denysenko, D.; Grzywa, M.; Baumgärtner, B.; Senkovska, I.; Kaskel, S.; Sastre, G.; van Wüllen, L.; Volkmer, D. CFA-1: The First Chiral Metal–Organic Framework

Containing Kuratowski-Type Secondary Building Units. *Dalton Trans.* **2013**, *42* (30), 10786–10797. DOI: 10.1039/c3dt50787d.
(105) Schmieder, P.; Grzywa, M.; Denysenko, D.; Hambach, M.; Volkmer, D. **CFA-7**: An Interpenetrated Metal–Organic Framework of the MFU-4 Family. *Dalton Trans.* **2015**, *44* (29), 13060–13070. DOI: 10.1039/C5DT01673H.
(106) Ravin, K.; Sarver, P.; Dinakar, B.; Palatinus, L.; Müller, P.; Oppenheim, J.; Dincă, M. High-Connectivity Triazolate-Based Metal–Organic Framework for Water Harvesting. *J. Am. Chem. Soc.* **2025**, *147* (13), 11407–11411. DOI: 10.1021/jacs.5c01062.
(107) Gu, L.; Xiong, Z.; Zhong, Y.; Chen, Z. Reticular Synthesis of High-Connectivity Metal–Organic Frameworks with Kuratowski-Type Building Blocks. *J. Am. Chem. Soc.* **2026**, *148* (1), 99–105. DOI: 10.1021/jacs.5c18835.

For Table of Contents Only